MASTER

Ellipsometry in beam etching

te Sligte, E.

Award date:
2001

Technische Universiteit Eindhoven
Faculteit Technische Natuurkunde
Capaciteitsgroep AQT/B

Ellipsometry in beam etching

E. te Sligte

Afstudeerverslag VDF/NO 01-02
April 2001

Begeleider: H. C. W. Beijerinck

Abstract

For a better comparison between plasma etching and beam etching, an ellipsometer is added to a multiple-beam setup in which Si is etched by XeF_2 and Ar^+ ions. An investigation of sputtering yields an ion damaged layer that can be described well with TRIM simulations, and a surface roughness of only 3 Å. Spontaneous etching is found to cause a rough reaction layer up to 13 nm thick. This cannot be distinguished from a thinner reaction layer on a rough surface. For ion-assisted etching, a two-layer model has been developed which describes the measurements satisfactorily. The reaction layer can be described by a Bruggeman mixture of rough a-Si and rough SiF_x. Its thickness can be described by an extrapolation of molecular dynamics simulation data. The amorphous layer thickness can be described well by the TRIM simulations.

Contents

1 Introduction **3**
- 1.1 Project motivation . . . 3
- 1.2 Experimental overview . . . 4
- 1.3 This report . . . 6

2 Ellipsometric theory **7**
- 2.1 Basic principle and conventions . . . 7
- 2.2 Effect of a thin film . . . 9
- 2.3 Impedance formalism . . . 9
- 2.4 Effective medium theory . . . 11
- 2.5 Comparison to other techniques . . . 12

3 SCEPTER **14**
- 3.1 Beam apparatus . . . 14
- 3.2 Ellipsometer . . . 16
  - 3.2.1 Principle . . . 16
  - 3.2.2 Realization . . . 17
- 3.3 Previous work with SCEPTER . . . 18
  - 3.3.1 Experimental results . . . 18
  - 3.3.2 Reaction model . . . 21

4 Article **24**
- 4.1 Introduction . . . 24
- 4.2 Reaction model . . . 25
- 4.3 Model of the amorphous layer . . . 26
- 4.4 Experimental . . . 29
  - 4.4.1 Vacuum apparatus . . . 30
  - 4.4.2 Ellipsometric theory . . . 30
  - 4.4.3 Ellipsometer . . . 32
  - 4.4.4 Measurement procedure . . . 33
  - 4.4.5 Influence of residual gas . . . 34
- 4.5 Sputtering . . . 34
  - 4.5.1 Time dependence . . . 34
  - 4.5.2 Steady state . . . 36
  - 4.5.3 Current dependence . . . 38
- 4.6 Spontaneous etching . . . 38
  - 4.6.1 Dose dependence . . . 39
  - 4.6.2 Surface model . . . 40

4.7 Ion-assisted etching: model 42
4.8 Measurements 44
4.8.1 Sputtering 44
4.8.2 Ion-assisted etching 44
4.8.3 Model sensitivity 45
4.8.4 Time dependence 47
4.9 Concluding remarks 49
4.9.1 Acknowledgements 49

A Software **52**
A.1 Reaction layer simulation 52
A.2 Ellipsometry simulation 53

B Technology assessment **55**

Chapter 1

Introduction

In this chapter, the motivation for this experiment is given. Further, a brief overview of the experiment is presented. The experimental setup is described in greater detail elsewhere [1]. The chapter concludes with a section describing the structure of this report.

1.1 Project motivation

In the last decades, integrated circuits (IC's) have become an integral part of life. They are at the heart of every computer or mobile phone and have been incorporated into cars, tv sets, and nearly all electrical appliances. In the production of IC's, etching is a crucial step. During etching, a pattern is introduced onto a semiconductor substrate, usually silicon. Until the end of the 1970's, this was done by letting the sample soak in a chemical solution for a while. This process, called *wet etching*, is isotropic. This imposes an limit of about one on the aspect ratio (height over width) of the structures that can be made, as can be seen in figure 1.1. From 1980 onwards, industry switched to *dry etching*. In this technique, the sample is placed in a vacuum environment. Subsequently, a plasma is generated at some distance (about 100 mm) from the sample. The sample is placed at a negative bias voltage. This causes the positive ions that exist in the plasma to be accelerated towards the sample. Reactive molecules and radicals (usually halogens, such as F) in the plasma diffuse towards the sample unhindered because of the low background pressure. While the neutral species in the plasma would etch isotropically, the ions cause a large increase in the etch rate in the vertical direction. This means that the process as a whole is strongly anisotropic. Aspect ratios as high as 120 have been attained with these etching methods [2].

In order to optimize the speed, efficiency, selectivity, and accuracy of the etching process, extensive research has been done [3]. Most of this research is done using the same types of plasma reactors that is used in etching practice. This approach, while close to application, entails some difficulties. As the plasma interacts with the surface, the reaction products cause a shift in the concentrations of various species in the plasma. These concentrations are what one actually measures, and the measurements are not easy or accurate. To obtain more insight into the reaction mechanics of the etch process, a more

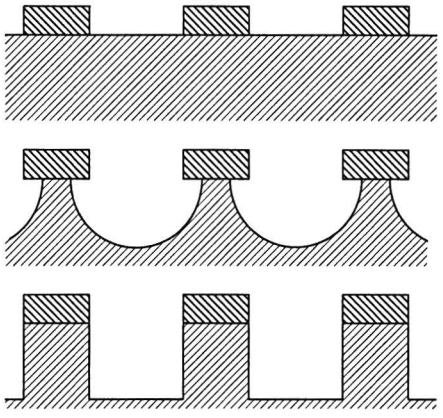

Figure 1.1: Difference between wet etching and dry etching. Top: sample with etching mask. Middle: sample after a wet etch treatment. Bottom: sample after a dry etch treatment.

direct method is necessary. One way to achieve this is by beam etching. In this technique the plasma is replaced by several beams, one for each etching agent. The fluxes to the sample are well-known, and the desorbing flux can be analyzed with the use of a mass spectrometer. One such setup is SCEPTER (Surface Chemistry Experiment for a Physical Theory of Etching Reactions) at Eindhoven University of Technology. This report is about experiments done with the SCEPTER setup.

1.2 Experimental overview

In the SCEPTER experiment, the plasma etching is simulated by various beams. A realistic plasma has reactive ions, nonreactive ions, electrons, radicals, molecules and etch products. For etching reactions, electrons are not relevant as they do not reach the sample because of the bias voltage. The etch products no longer react with the surface, and therefore are not of interest to us. Reactive ion beams are not experimentally feasible due to the intense corrosive effect that the ions would have on the equipment that generates the beam. This leaves us with nonreactive ions, molecules and radicals.

The nonreactive ion beam consists of argon ions. This is because the ions reach maximum efficiency when their mass is about equal to the mass of the other atom species present in the etching process. This condition is met in the cheapest way possible by using argon ions.

Radicals are rather difficult to make as a beam with a well-defined energy. Although good radical beam sources do exist at present, technology at the time of the construction of this setup did not allow for such a beam to be incorporated into the experiment. The radicals are necessarily replaced by a beam of molecules. By using very weakly bound molecules, etching can still be achieved. Most molecules do not produce spontaneous etching reactions on silicon simply because the energy needed to break both the molecular bond and

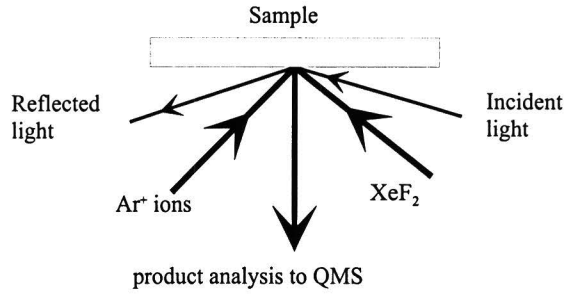

Figure 1.2: Configuration of the various beams relative to the sample surface. The ellipsometer is out of plane by 30° and the XeF_2 beam by 135°. The angle of the ellipsometer laser beam has been chosen for optimum sensitivity.

the Si-Si crystalline bond is greater than that released when the etch products are formed. In all cases, etching can only occur with a species that has a higher binding energy to Si than Si itself. The etch product must also spontaneously desorb into the gaseous phase at room temperature. There are four such species, H, F, Cl, and Br. The F radical is the most reactive and therefore the most commonly used. The most weakly bound molecule containing F is XeF_2. It is held together by Van der Waals forces only. We consider this molecule a good substitute for F radicals, as the fluorine is free to react with the silicon and spontaneous etching with XeF_2 does occur.

As the XeF_2 and Ar^+ beams etch the silicon sample, the etch products (mainly SiF_2 and SiF_4) desorb from the sample. The etch products are then analyzed with a quadrupole mass spectrometer (QMS). A host of experiments have already been done with the QMS, leading to a model that will be discussed in section 3.3.2. The main characteristics of the dynamics of this process are well-understood. The problem that we face now is bridging the huge gap between the beam experiments and the practice of plasma etching.

To achieve just that, an ellipsometer has been added to the experimental setup [5, 6]. In ellipsometry, one investigates a surface by measuring the change in polarization that a light beam undergoes during reflection at the surface. Ellipsometry is a non-invasive technique that can be used *in-situ*, requires little time and is extremely accurate. Its disadvantage, however, is that the sensitivity to the specific details of the multilayer model used is very large. Without sufficient input data from other measurements, this can lead to rather arbitrary models. Ellipsometry is described in greater detail in section 3.2.

This report is about experiments that have been performed with the ellipsometer to characterize the reaction layer during ion-assisted etching. The parts on etching in the absence of ions and pure sputtering (without XeF_2) draw largely on previous work by Sebel [1], Mestrom [5] and Driessen [6]. The ultimate goal is to find a model that will explain the characteristics of the etching process as examined with the mass spectrometer and the ellipsometer. It is expected that adapting the results of this study to plasma etching in practice will be fairly straightforward. The setup of the beams used in this experiment is depicted in figure 1.2.

1.3 This report

The heart of this report is a paper for the Journal of Vacuum Science and Technology A that is based on the results of the author's MSc graduation project. In order to keep the workload within acceptable bounds for the graduation project, the paper has been copied into this report as is. The remainder of the report is a more detailed explanation of this paper, intended to bring the level of detail and the familiarity required of the reader closer to the standards that are accepted for TU/e graduation reports.

In chapter 2, a more detailed description of the theory of ellipsometry will be given. A description of the model for the etching reaction and the experimental setup will be given in chapter 3. This should give the reader all necessary knowledge to read the article, which will be incorporated as chapter 4. Listings of software written in the course of this project will be given in appendices.

Chapter 2

Ellipsometric theory

Ellipsometry is a measurement technique that is based on the analysis of the polarization of a light wave. A polarized light wave is created. It reflects from the surface to be investigated. The polarization of the reflected wave is analyzed to characterize of the surface under investigation. In this section, we will first go into the basics of ellipsometry. Then we will discuss the effect of a film on the surface, and the effect of several films. We will then discuss methods for modelling materials that are a mixture of several components. We will end this section by an analysis of the advantages and disadvantages of ellipsometry.

2.1 Basic principle and conventions

Light consists of electromagnetic waves. The electric and magnetic fields have perpendicular orientation with respect to each other (figure 2.1). The electric field can be broken down into a superposition of two plane waves, with one plane wave polarized parallel to the plane of incidence (called p) and the other perpendicular to that plane (called s for German *senkrecht*). According to the Fresnel laws [7], both these waves will have a different amplitude reflection coefficient:

$$\begin{aligned} r_p &= \frac{E_p^r}{E_p^i} = \frac{\tilde{n}_1 \cos\theta_0 - \tilde{n}_0 \cos\theta_1}{\tilde{n}_1 \cos\theta_0 + \tilde{n}_1 \cos\theta_1} \\ r_s &= \frac{E_s^r}{E_s^i} = \frac{\tilde{n}_0 \cos\theta_0 - \tilde{n}_1 \cos\theta_1}{\tilde{n}_0 \cos\theta_0 + \tilde{n}_1 \cos\theta_1} \end{aligned} \tag{2.1}$$

In these equations, the superscripts i and r stand for *incident* and *reflected*, respectively. The angle of incidence is called θ_0, the angle of transmission θ_1. The complex refractive indices of the media are called $\tilde{n}_0$ and $\tilde{n}_1$. The complex refractive index of each medium can be written as:

$$\tilde{n}_i = n_i + jk_i, \tag{2.2}$$

with $i = 0, 1$ and n_i and k_i the real and imaginary parts of the refractive indices, respectively. The real part of the refractive index of any medium will be greater than one, otherwise the light would be accelerated to more than light speed by the presence of the medium. Under nearly all circumstances, k will be negative. This is because k represents the absorption by the medium. It is related to the

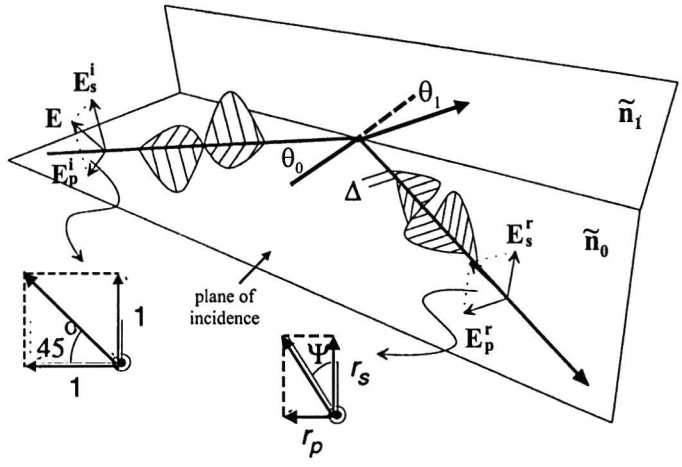

Figure 2.1: The effect that angles Ψ and Δ have on a wave consisting of two orthogonally polarized components. The incoming wave has zero phase shift between and unity amplitude ratio between the two. In the outgoing wave, the amplitude ratio is $\tan\Psi$, and the p-component has been retarded by a phase angle Δ.

absorption coefficient α by:

$$\alpha = \frac{4\pi k_i}{\lambda_0}, \tag{2.3}$$

with λ_0 the wavelength of the light. The absorption coefficient is defined by the intensity $I(d)$ that a light beam of intensity I_0 has after propagating a distance d through a material:

$$I(d) = I_0 e^{\alpha d}. \tag{2.4}$$

This system can be solved by using Snell's law to determine θ_1:

$$n_0 \sin\theta_0 = n_1 \sin\theta_1. \tag{2.5}$$

With the Fresnel equations (2.1), we can define a new quantity ρ:

$$\rho \equiv \frac{r_p}{r_s}. \tag{2.6}$$

The quantity ρ is a measure for the change in polarization of the electromagnetic wave. It is usually written in polar form. The amplitude is expressed as the tangent of an angle Ψ and its phase angle is dubbed Δ:

$$\rho \equiv \tan\Psi e^{j\Delta}. \tag{2.7}$$

Convention dictates that both Ψ and Δ be expressed in degrees, with Ψ between 0° and 90° and Δ between 0° and 360° . A possible interpretation for the angles Ψ and Δ is given in figure 2.1.

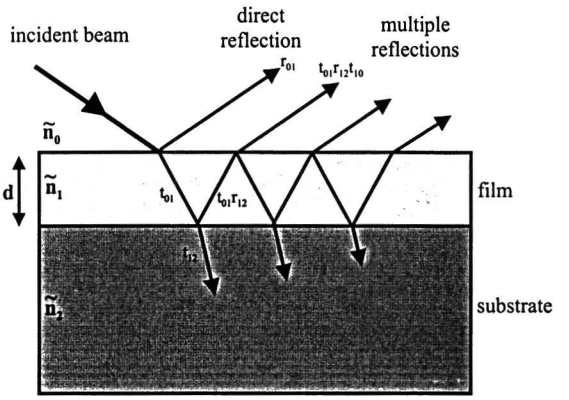

Figure 2.2: Multiple reflection on a surface with a film of thickness d on top. Also indicated are the coefficients of reflection and transmission.

2.2 Effect of a thin film

In the case of reflection from a substrate with a thin homogeneous film on top, we find that the situation is complicated by the multiple internal reflections that occur (see figure 2.2). First, we investigate the effect that propagation through the film has on the light wave [7] of wave number k:

$$\vec{E}_{end} = \vec{E}_{begin} e^{-j\tilde{n}kd\cos\theta_1} \equiv \vec{E}_{begin} e^{-j\beta}. \tag{2.8}$$

This introduces the *phase thickness* β, the (complex) phase shift undergone by the wave during propagation through the film. Further we introduce the reflection coefficient r_{ij} from medium i with refractive index $\tilde{n}_i$ to medium j with refractive index $\tilde{n}_j$, and analogous transmission coefficients t_{ij}. This means that we get, for the total reflection coefficient r_t:

$$\begin{aligned} r_t &= r_{01} + t_{01}e^{-j\beta}r_{12}e^{-j\beta}t_{10} + t_{01}e^{-j\beta}r_{12}e^{-j\beta}r_{10}e^{-j\beta}r_{12}e^{-j\beta}t_{10} + \dots \\ &= r_{01} + t_{01}t_{10}r_{12}e^{-2j\beta}[1 + r_{10}r_{12}e^{-2j\beta} + (r_{10}r_{12}e^{-2j\beta})^2 \dots]. \end{aligned} \tag{2.9}$$

Using $r_{01} = -r_{10}$ from equation 2.1 and conservation of energy in the form $t_{01}t_{10} = 1 - r_{01}^2$, we get a total reflection coefficient r_t

$$r_t = \frac{r_{01} + r_{12}e^{-2j\beta}}{1 + r_{01}r_{12}e^{-2j\beta}}. \tag{2.10}$$

In this way, we can calculate both the amplitude reflection coefficients R_p and R_s. This can be used to calculate the ellipsometric angles Ψ and Δ:

$$\rho \equiv \tan\Psi e^{j\Delta} = \frac{r_{t,p}}{R_{t,s}}. \tag{2.11}$$

2.3 Impedance formalism

In the case of several thin films covering a surface, the calculus becomes exponentially more unwieldy, as all internal reflections in all layers must be taken

into account. There is a more elegant solution to this problem than crunching numbers: the impedance formalism. In the impedance formalism, we introduce two impedance factors (one for each polarization) per medium. For medium i, they are defined as:

$$\begin{aligned} f_{pi} \equiv \quad \frac{\cos\theta_i}{\tilde{n}_i} \quad &= \frac{\sqrt{\tilde{n}_i^2 - \tilde{n}_0^2 \sin^2\theta_0}}{\tilde{n}_i^2} \\ f_{si} \equiv \quad \tilde{n}_i \cos\theta_i \quad &= \sqrt{\tilde{n}_i^2 - \tilde{n}_0^2 \sin^2\theta_0}. \end{aligned} \tag{2.12}$$

Medium 0 is the medium in which the light wave originates. In this report, medium 0 will always be vacuum. There may be no direct boundary between the media 0 and i, but the media can still be compared. With the use of equation (2.12), we can rewrite the Fresnel equations (2.1) to give:

$$r_p = \frac{f_{p0} - f_{p1}}{f_{p0} + f_{p1}}, r_s = \frac{f_{s0} - f_{s1}}{f_{s0} + f_{s1}}. \tag{2.13}$$

One advantage of this formalism already appears: both polarizations are treated identically. The phase thickness of each film can also be calculated:

$$\beta_i \equiv \frac{2\pi}{\lambda} d_i n_i \cos\theta_i = \frac{2\pi}{\lambda} f_{si} d_i \tag{2.14}$$

From now on the subscripts p and s will be suppressed, as the mathematical treatment of the problem is identical for both polarizations.

If we now introduce a new parameter u, given by:

$$u \equiv r_{21} e^{-2j\beta_2} = \frac{f_2 - f_1}{f_2 + f_1} e^{-2j\beta_2}, \tag{2.15}$$

we get a new expression for the total reflection coefficient r_t:

$$r_t = \frac{r_{02} + u}{1 + r_{02} u}. \tag{2.16}$$

We now want to calculate the effective impedance f_x of the substrate-plus-film ensemble. We can get this from the reflection coefficient, by noting that the reflection coefficient $r_t = r_{0x}$ has to obey the Fresnel equations in the form (2.13). This gives us a total impedance

$$f_x = f_2 \frac{1 - u}{1 + u}. \tag{2.17}$$

We now have the effective impedance for the substrate with thin film. If there are two films, the previous calculation is repeated using the total impedance f_x as the substrate impedance in a system with a single thin film. The method is illustrated in figure 2.3. This is the main advantage of the impedance algorithm: extra films on the surface are easily included in the calculations.

From the effective impedance factor f_x for the substrate-plus-films ensemble, we can get the total reflection coefficient at the top layer:

$$r_{0x} = \frac{f_0 - f_x}{f_0 + f_x}. \tag{2.18}$$

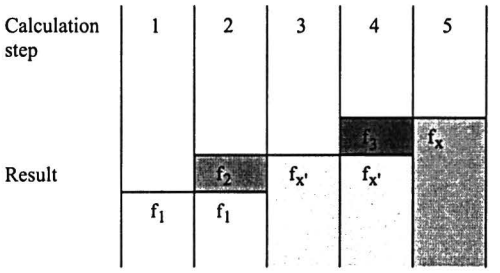

Figure 2.3: Method for calculating the reflection coefficients for a multiple-film situation: (1) impedance of the substrate is calculated; (2) impedance and phase thickness of the lowest-lying film are calculated; (3) effective impedance of the substrate plus one film is calculated; (4) impedance and phase thickness of the lowest-lying film are calculated; (5) impedance of the whole system is calculated, and the subsequently the reflection coefficient.

This ratio can be calculated for both the p and s polarizations. From the results, the ellipsometric angles Ψ and Δ can be calculated:

$$\rho = \frac{r_{p0x}}{r_{s0x}} = \tan\Psi e^{j\Delta}. \tag{2.19}$$

This algorithm has been implemented in a simulation program called *ellsim* that has been developed by Kroesen *et al.* at TU/e [11]. This program or its calculating routines are used for all simulations of ellipsometric measurements in this report.

2.4 Effective medium theory

Sometimes a medium consists of two components that do mix but do not influence each other. In this case, the refractive index of neither one nor the other gives a good description of the optical properties of the mixture. The best way to describe this is by introducing an *effective medium*, with optical properties that result from both constituents. Examples of such media include rough surface layers, porous media, and surfaces covered with two different materials. The approximation of an effective medium is valid as long as the variations in optical properties occur on length scales that are small compared to the wavelength of the light used. This means that there is an upper boundary of about $\lambda/10$ to the size of the inhomogeneities. In this report, that boundary will be at 63 nm, and the homogeneity requirement will be satisfied easily at all times.

There are various models to describe effective media [8]. These include the Lorentz-Lorenz model, which describes dipolar molecules in vacuum, the Maxwell-Garnett model, which describes inclusions in a non-vacuum medium, and the Bruggeman model [33]. The Bruggeman model describes several components that constitute one effective medium. The Bruggeman model couples the dielectric constants of the various materials in the Bruggeman equation [8]:

$$0 = \sum_{i=1}^{n} V_i \frac{\epsilon_i - \epsilon_e}{\epsilon_i + 2\epsilon_e}. \tag{2.20}$$

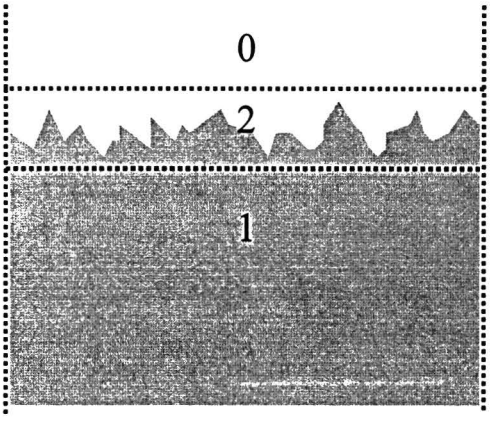

Figure 2.4: Ellipsometric modelling of a rough surface. The boundary between media 0 and 1 is modelled as a separate layer 2. The refractive index of layer 2 is determined by the Bruggeman equation.

There are a total n constituent materials, with dielectric constants ϵ_i occupying volume fractions V_i. The effective medium has dielectric constant ϵ_e. As we are primarily interested in the refractive index of the effective medium, we want to express this equation in terms of refractive indices. This can be done with the relation $\epsilon = \tilde{n}^2$ [9]:

$$0 = \sum_{i=1}^{n} V_i \frac{\tilde{n}_i^2 - \tilde{n}_e^2}{\tilde{n}_i^2 + 2\tilde{n}_e^2}. \tag{2.21}$$

One of the most common uses for effective medium theory is to predict the refractive index of a rough surface layer. The thickness of this layer is usually unknown, as are the volume fractions of the constituent media. The most common way of modelling these media is by assuming that they are made up of material and roughness in a 50/50 volume ratio. This is essentially a random value, but it is a random value that is sure to generate reasonable values for surface roughnesses.

2.5 Comparison to other techniques

Ellipsometry as a surface diagnostic has various advantages. One major advantage to ellipsometry is its non-destructive nature: the light that is used (usually a few mW of red or infra-red light) has little or no effect on the processes that are studied. In comparison with other surface analysis techniques such as LEIS and LEED, which use particles that have energies in the keV range, their effect is certainly negligible. Furthermore, ellipsometry is relatively fast. Measurements can be taken in a fraction of a second. This means that it can be used to monitor surfaces in real time in actual etching environments. This is called *in situ* ellipsometry. Third, ellipsometry is highly accurate. It is capable of detecting submonolayer concentrations of surface pollutants. This means that it can be used to gain a very accurate image of the surface in question. Another

advantage that ellipsometry has over most surface analysis methods is that it is quite cost-effective. The necessary components are a laser, a few polarizing filters plus mounts, a photodiode and a computer. This is available at relatively low cost.

There are also disadvantages to ellipsometry as a study method. The greatest disadvantage of all is probably the fact that there is no straightforward way to relate the measured quantities, Ψ and Δ, to actual properties of the surface under investigation such as layer thicknesses or refractive indices. This has to be done via a computer simulation. This simulation requires at least educated guesses as to the composition of the surface as input. For a two film situation, that means that at least four parameters must be known beforehand. That is not always feasible.

All this means that ellipsometry is not much use if you do not yet have a fairly good idea of what you are studying. If you do have prior knowledge of the surface under investigation, it is one of the most accurate, robust and effective techniques there are.

Chapter 3

SCEPTER

The goal of this work is the study of etching reactions. The experimental setup that was used in this report is called SCEPTER. It will be described in the following section; further details can be found in previous reports [5, 1, 4, 10] . SCEPTER has been in operation for about ten years at the time of this report. During this time, a host of experiments have been performed. The main results and insights gained from these experiments will be summarized in the following section.

3.1 Beam apparatus

An overview of the setup is shown in figure 3.1. The samples are introduced into a load lock. The samples can be transferred from the load lock to the sample chamber, where the experiments take place. The quadrupole mass spectrometer is located in another vacuum chamber, with two flow resistances in between.

The load lock is pumped by a 56 l/s turbomolecular pump. This gives a base pressure of $1 \cdot 10^{-8}$ mbar. The load lock is separated from the sample chamber by a valve. This allows the samples in the load lock to be replaced while leaving the vacuum in the sample chamber undisturbed. Transfer of the samples between the load lock and the sample chamber is possible through a magnetic linear drive.

The sample chamber is the section of SCEPTER where the experiments take place. To supply all the beams to the sample, a hemispherical central flange was made. The sample is at the center of the hemisphere. The various beam sources were fitted onto the flange. The sample chamber is pumped with two turbomolecular pumps in series, of pumping speeds 500 l/s and 50 l/s. This results in a base pressure of $5 \cdot 10^{-8}$ mbar. This pressure increases to the order of $1 \cdot 10^{-6}$ mbar if the XeF_2 beam or the Ar^+ beam are in use.

The sample holder can hold two samples, usually one of Si (for the etching experiments) and one of Ni. The Ni sample serves as an inert reference for calibration of the mass spectrometer (see section 3.3.1). The sample can be heated up to 900 K [5].

Before we go into the specific characteristics of the beams, it is necessary to define the unit of surface density that will be used throughout this report: the monolayer (ML). One monolayer is defined as the surface density for silicon

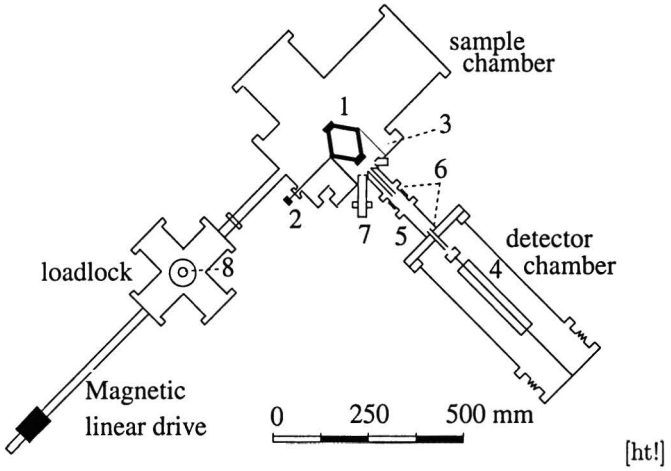

Figure 3.1: The SCEPTER setup in horizontal cross-section. Up to six samples can be stored in a load lock. The sample is mounted in a sample holder (1) that can be rotated by a manual drive (2). All beams directed at the sample are mounted into a central spherical flange (3). The vacuum in the mass spectrometer (4) is separated from that in the sample chamber by two differential pumping stages (5) and two flow resistances (6). The ions are produced by an ion gun (7). The desorbing etch products are analyzed with a mass spectrometer (4). A supply of up to six samples can be stored in the load lock (8). The XeF_2 source and the ellipsometer are not depicted as they are outside the horizontal plane.

[100]. In SI units:

$$1\text{ML} = 6.86 \cdot 10^{18}\text{m}^{-2}. \tag{3.1}$$

All flux densities will be expressed in ML/s.

The argon ion beam is generated using a Kratos WG537 Macrobeam ion gun. The ion beam produced is Gaussian to a good approximation, having a FWHM of 5 mm. The energy of the ions can be varied between 0.2 keV and 2.5 keV. The ion current that can be generated varies between one μA for 0.5 eV ions and ten μA for 2 keV ions. The alignment of the ion beam can be adjusted with a set of deflector plates in order to ensure that the ion beam hits the sample. The ion current can be converted into the ion flux density on the sample by a conversion factor: 1 μA ion current is equivalent to 0.011 ML/s ion flux density.

Xenon difluoride is a crystal at room temperature. We are able to use such a crystal as a gas source because it has a vapor pressure of 5 mbar at room temperature [10]. This vapor pressure can be reduced by about a factor of thirty by cooling the reservoir to 0°C. The use of a capillary allows the flux passing through the inlet system to be known by calculation. We can now control the flux of XeF_2 that we introduce into the sample chamber. The beam is made highly directional by the use of a multichannel array. The resulting gas inlet system has a flux range of 0.06 ML/s (at maximum cooling) to 3.6 ML/s at room temperature.

The mass spectrometer is separated from the sample chamber by two flow resistances. These ensure that 85 % of the flux that enters the mass spectrometer has directly desorbed from the sample, and has not had any collisions with walls in between. Furthermore, they preserve the vacuum in the mass spectrometer chamber, which is better than in the sample chamber. The base pressure in the mass spectrometer is $4 \cdot 10^{-9}$ mbar. This low base pressure is needed in order to provide a sufficient signal-to-background ratio. The signal-to-noise ratio in the mass spectrometer is about 30, with a background noise in the order of 0.7 kHz and signal strengths around 20 kHz.

3.2 Ellipsometer

We want to be able to determine the ellipsometric angles Ψ and Δ. This section serves to explain how that is done. First, the basic principle will be explained. For a mathematical analysis, the reader is referred to Mestrom [5]. In the second part of this section, the experimental realization will be discussed. We will only discuss the components of the setup, for a thorough analysis of how to calibrate and use the setup, the reader is referred to Mestrom [5].

3.2.1 Principle

The ellipsometric measurements are done with laser light. It is initially linearly polarized. Because we want to perform measurements with the polarization of our choice and not with that of the laser's choice, we have installed a $\lambda/4$-retarder. This retards part of the laser light, so that circularly polarized light exits it if linearly polarized light goes in. The circularly polarized light is then reconverted to linear light with polarization vector defined by the polarizer. The intensity of the linearly polarized light is independent of the orientation of the

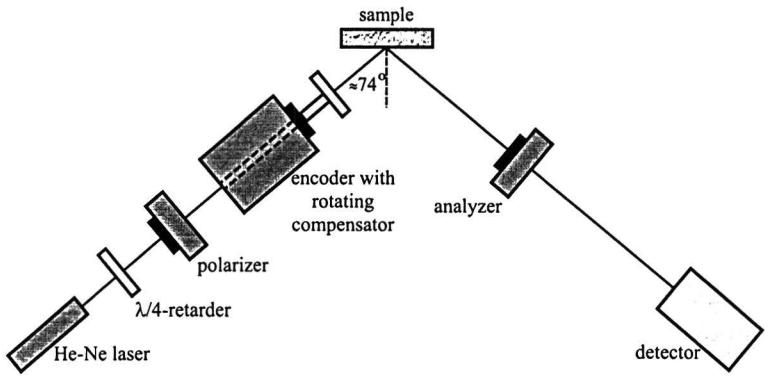

Figure 3.2: The experimental setup for the ellipsometry measurements.

polarization filter. The linearly polarized light now passes through a second $\lambda/4$-retarder, called the compensator. This $\lambda/4$-retarder changes the polarization and intensity of the linearly polarized beam depending on its orientation. Because the sample has different reflection coefficients for both polarization directions, the signal leaving the sample has a polarization and an intensity that depend on the compensator orientation and the sample properties. This light is then passed through an analyzer in order to translate the variations in polarization into intensity variations. We now have a total signal that varies in intensity as a function of the sample properties and the compensator orientation. This signal is then detected by a photodiode. To extract the sample properties Ψ and Δ, the signal is measured for all orientations of the compensator. In practice, this is done by letting the compensator rotate at a fixed frequency. This results in a periodic signal. The signal is Fourier-analyzed. From the Fourier components, the ellipsometric angles Ψ and Δ can be extracted.

3.2.2 Realization

In figure 3.2, a schematic overview of the ellipsometric setup is given. The laser light used is produced by a Melles Griot 05-LHP-111 Helium-Neon laser at a wavelength of 632.8 nm. The beam emitted by this laser is 0.59 mm thick, and has a divergence of 1.35 mrad. The laser power is 1 mW. The laser light is highly polarized. The polarization ratio is at least 500 to 1.

The laser light is converted to circularly polarized laser light by a $\lambda/4$-retarder (Melles Griot 02-WRM-011). The retarder is a mica sheet 10 mm in diameter. It has been mounted in a rotatable mount so it can be rotated around the laser beam to get the right polarization. The resulting laser light is circular to within 10 %. This is not a problem in measurement as the orientation of the polarizer does not change during measurement.

The polarizer is a homogeneous dichroic sheet polarizer (Melles Griot 05-FPG-001) and has also been mounted on a rotatable mount. It can be adjusted to an accuracy of 0.02°. The polarizer has an extinction coefficient for its nontransmissive axis of 10^4. This is more than enough, as we are not able to read our signal to such accuracy. The analyzer is identical to the polarizer.

The compensator is a $\lambda/4$-retarder made of quartz (Döhrer Elektrooptik WZQ 150-633). It is 10 mm across and has a non-polarizing antireflection coating. Experimental comparison to compensators without this anti-reflective coating has shown that this coating is a necessity [5]. The compensator rotates at 33 Hz as dictated by the maximum processing speed of the computer system.

The encoder is a part of the detection system. It generates the trigger pulses for the detector readout. It generates these pulses at the start of every rotation and at 256 regular intervals during every rotation. The pulses are generated at regular intervals of angle so the measurement does not suffer from frequency variations in the rotational speed of the compensator.

The detector is a photodiode with a simple amplification scheme. The amplification is necessary in order to ensure optimum utilization of the readout accuracy of the 12-bit ADC (Analog-to-Digital Converter). The ADC reads the photodiode signal at every trigger pulse. From there on, the signal is fed into a computer system, where the ellipsometric angles are determined from the Fourier coefficients of the signal.

3.3 Previous work with SCEPTER

The SCEPTER project has been in operation for about ten years, yielding two PhD theses [4, 1]. A brief overview of this work is given below. First, we will treat the chief experimental results of the etching experiments. This will be followed by a discussion of the model that has been derived from these results.

3.3.1 Experimental results

The experimental results treated here were obtained with the use of the mass spectrometer only. The mass spectrometer can be used to detect particle fluxes only. With the use of an inert Ni reference sample, the fluxes that desorb from the sample can be calibrated absolutely. This results in several measurable quantities. From the XeF_2-flux from the sample, it is possible to measure the chance that *something* happens to the XeF_2 at the sample. This reaction probability ϵ is defined as [4]:

$$\epsilon \equiv \frac{\Phi(XeF_2)_s - \Phi(XeF_2)}{\Phi(XeF_2)_s}, \tag{3.2}$$

where $\Phi(XeF_2)$ is the XeF_2-flux desorbing from the sample and $\Phi(XeF_2)_s$ is the XeF_2-flux onto the sample. With the use of the mass spectrometer, it is also possible to determine the composition of the etch products. The quantities measured here are the amounts of Si_xF_y species produced per incident XeF_2-molecule. If $x > 1$, a silicate chain desorbs from the surface. This was not found in measurable quantities and therefore will be assumed to be a nonexistent process in the following. The etch product distribution thus consists of SiF, SiF_2, SiF_3, and SiF_4. In the case of spontaneous etching (just XeF_2, no ions) the etch products were found to consist exclusively of SiF_4 at temperatures below 600 K. The lesser-fluorinated SiF_x species were produced only by sputtering processes. For ease of modelling, all these species will be considered as one category, and be taken to be "SiF_2". This is a crude approximation, but a necessary one, as the SiF_x species cannot be told apart absolutely by the mass spectrometer. The

problem here is that SiF_x can be ionized to give SiF^+_{x-1}, and that this process is not suppressible. For purposes of modelling, this results in two different production coefficients for SiF_4 and SiF_2:

$$\begin{aligned} \delta_4 &\equiv \frac{4\Phi(SiF_4)}{2\Phi(XeF_2)_s}, \\ \delta_2 &\equiv \frac{2\Phi(SiF_2)}{2\Phi(XeF_2)_s}. \end{aligned} \tag{3.3}$$

Here the SiF_x flux desorbing from the sample is called $\Phi(SiF_x)$.

When performing these measurements, there are several parameters that can be varied: the ion flux, the XeF_2 flux, and the sample temperature. Variation of the ion flux and the XeF_2 flux turns out to have an effect that depends solely on the ratio of the two fluxes, as can be seen in figure 3.3. This means that the model description of the etching process will have to be in terms of this flux ratio R, defined as:

$$R \equiv \frac{\Phi(Ar_s^+)}{\Phi(XeF_2)_s}. \tag{3.4}$$

The effect of the ions is to enhance greatly the reaction probability, from about 10 % in the case of spontaneous etching to over 80 % for high flux ratios. This means that the ions cause a change in the surface of the sample that makes XeF_2 react better. Measurements of δ_x indicate that, for spontaneous etching, the production of anything but SiF_4 is negligible at room temperature. In the case of ion-assisted etching, there is significant SiF_2 production. These less-fluorinated species in ion-assisted etching are due to sputtering. The idea of sputtering is that a highly energetic particle (usually an ion) hits the sample and causes a collision cascade. Because of this cascade, some particles are bounced out of the surface. This is easier for particles with a lower binding energy. As a result, the silicon is left more or less in place, while the ions are very efficient in removing the SiF_x species.

Variation of the sample temperature gives a rather surprising effect: the reaction probability decreases with increasing temperature, as can be seen in figure 3.4. In order to explain this, there must be a process that limits the reaction probability that becomes more important with higher temperature. The XeF_2 is normally crystalline at room temperature, and has a vapor pressure that increases with temperature. Thus it is very possible that the XeF_2 remains in an adsorbed phase for a certain time. This state is called the *precursor* state. During this time, it is physically bound (also called "physisorbed") to the surface by Van der Waals forces. After a while, it evaporates. This evaporation process would naturally speed up with increasing temperatures. Reaction of the XeF_2 with the surface can only occur during while it is physically adsorbed. Therefore the reaction probability would decrease with increasing temperature, as observed. The temperature dependence of the reaction probability leads to an evaporation energy of 32 meV [1].

Further evidence for the existence of the precursor state can be found in that the reaction probability for F radicals with a silicon substrate is several orders lower than the 10 % for XeF_2 [2]. The energy balance is more favorable for F radical reaction with the substrate, so there must be a mechanism that enhances the reaction probability for XeF_2. A longer residence time at the surface because of precursor formation then sounds quite logical.

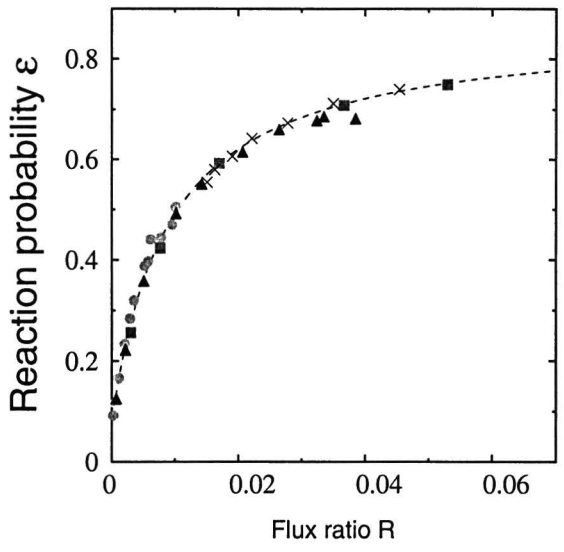

Figure 3.3: The dependence of the reaction probability ϵ on the flux ratio R, measured at room temperature (300 K); The XeF_2 flux varies from 0.034 ML/s to 3.4 ML/s. (Taken from Vugts [4])

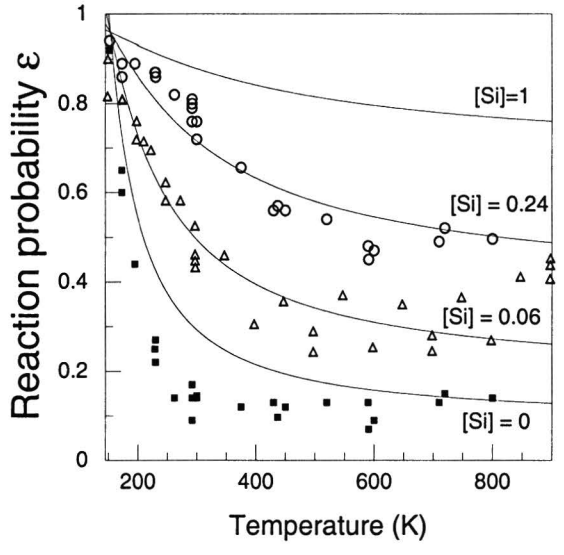

Figure 3.4: The temperature dependence of the reaction probability ϵ for various ion-to-neutral flux ratios (Taken from Sebel [1]). The measurement data are for ion to neutral flux ratio 0 (squares), 0.012 (triangles), and 0.025 (circles). The drawn lines indicate model fits for a XeF_2 desorption energy of 32 meV and a fixed fraction of bare Si.

3.3.2 Reaction model

In this section, we detail the model that describes the observed characteristics of the etching reaction of XeF_2 and Ar^+ on Si. The assumptions made here are:

1. Although the reaction layer consist of SiF_x species, it can be described as a mixture of Si and SiF_2 species only.
2. The reaction occurs at room temperature.
3. Any surface roughening that may occur will not affect the reaction probabilities in any appreciable way. This means that the reaction is not determined by the amount of surface available for reaction, but by the composition of the surface.

The first step is that the incoming XeF_2 is adsorbed into a precursor (p) state. This precursor state is defined as being close enough to the surface to react with it. The XeF_2 remains in this state for an average time τ before desorbing:

$$XeF_{2(g)} \overset{\tau}{\leftrightarrows} XeF_{2(p)} \tag{3.5}$$

The second step is the reaction of the XeF_2 with a surface species. This surface species can either be a fluorinated site or a Si atom. In the case of a reaction with a Si atom, the reaction coefficient is dubbed k_s; the reaction with a fluorinated site occurs with reaction coefficient k_f. As the reaction layer model is currently meant for room temperature only, the direct desorption of SiF_2 can be ignored. Thus spontaneous etching occurs via the reaction path:

$$\begin{aligned} XeF_{2(p)} + Si_{(s)} &\xrightarrow{k_s} SiF_{2(s)} + Xe_{(g)} \\ XeF_{2(p)} + SiF_{2(s)} &\xrightarrow{k_f} SiF_{4(g)} + Xe_{(g)} \end{aligned} \tag{3.6}$$

If the argon ions react with a bare Si surface species, they can sputter it. If they do so, a Si site is replaced by another Si site. The only possible effect is surface roughening, which is neglected in this model. Therefore, this reaction is disregarded.

The reaction of the argon ions with a SiF_2 surface species is more relevant to our model. If a SiF_2 species is physically sputtered, it leaves the surface directly, leaving a Si site in its place. If it is chemically sputtered, it is excited into a reactive state and reacts so fast that it effectively leaves the surface immediately as SiF_4. The chemically sputtered species also leave a Si site. In the models of Vugts and Sebel, the sputtering chances are defined in terms of a fluorine balance, whereas here they come from a silicon balance. This causes our sputtering chances to be exactly half of their sputtering chances. The numbers of either of these reactions caused per ion are $\frac{1}{2}p_c$ and $\frac{1}{2}p_p$, respectively:

$$\begin{aligned} SiF_{2(s)} + Ar^+ &\xrightarrow{\frac{1}{2}p_p} SiF_{2(g)} + Ar^+ \\ SiF_{2(s)} + Ar^+ &\xrightarrow{\frac{1}{2}p_c} SiF_{4(g)} + Ar^+ \end{aligned} \tag{3.7}$$

With this set of reactions, it is possible to construct the balance equations for the XeF_2 precursor concentration $\mathcal{X}$ and the fluorinated-sites fraction $\mathcal{F}$. The balance for the bare Si fraction $\mathcal{S}$ does not need to be made up, as every

destruction of a dangling bond equals creation of a fluorinated site and vice versa. The incoming XeF_2 flux is labelled Φ and the ion current is dubbed $\mathcal{I}$. The resulting equations are:

$$\begin{array}{rcccccc} 0 = \frac{\partial \mathcal{X}}{\partial t} & = & +\Phi & -\frac{\mathcal{X}}{\tau} & -\mathcal{X}\mathcal{S}k_s & -\mathcal{X}\mathcal{F}k_f & -\mathcal{F}\mathcal{I}\frac{1}{2}p_c \\ 0 = \frac{\partial \mathcal{F}}{\partial t} & = & & & +\mathcal{X}\mathcal{S}k_s & -\mathcal{X}\mathcal{F}k_f & -\mathcal{F}\mathcal{I}\frac{1}{2}p_p \quad -\mathcal{F}\mathcal{I}\frac{1}{2}p_c \end{array} \tag{3.8}$$

If we rewrite both of these equations to give two expressions for $\mathcal{X}$, this gives us:

$$\begin{array}{rcl} \mathcal{X} & = & \frac{(\Phi - \mathcal{I}\mathcal{F}\frac{1}{2}p_c)\tau}{1 + \mathcal{S}k_s\tau + \mathcal{F}k_f\tau} \\ \mathcal{X} & = & \frac{\mathcal{I}\mathcal{F}(\frac{1}{2}p_p + \frac{1}{2}p_c)}{\mathcal{S}k_s - \mathcal{F}k_f} \end{array} \tag{3.9}$$

Equating these two expressions and keeping in mind that, in the absence of roughness, $\mathcal{S} + \mathcal{F} = 1$, gives an equation linking $R = \mathrm{I} \ / \ \Phi$ to the bare Si fraction $\mathcal{S}$:

$$\begin{array}{ll} (1 - R(\frac{1}{2}p_c + \frac{1}{2}p_c\mathcal{S})) & (-k_f\tau + (k_s\tau + k_f\tau)\mathcal{S}) = \ldots \\ R(\frac{1}{2}p_p + \frac{1}{2}p_c) & (1 - \mathcal{S})(1 + k_f\tau + (k_s\tau - k_f\tau)\mathcal{S}) \end{array} \tag{3.10}$$

All other parameters have been measured in previous experimental work, and those results are summarized in table 3.1. Sebel *et al.* [1] find very different values for most coefficients than do Vugts *et al.* [4]. The cause for this difference is most likely in the different doping levels that they use. Both use n-type, P-doped [100] Si wafers, but Sebel *et al.* uses samples with a resistivity of 30-70 Ω-cm, whereas Vugts *et al.* have a resistivity of only 2-3 Ω-cm. The present experiment is performed using samples at a doping of 10 Ω-cm, so the values for the reaction coefficients are chosen as the average of the previously reported values.

The equation is clearly quadratic in $\mathcal{S}$, so the solution $\mathcal{S}$ will have the form of the abc-formula. In this formula terms a, b, and c will be first order polynomials of R. This can be plotted and calculated with the use of mathematical software like MAPLE. This plot is shown for the average reaction coefficients in figure 3.5. The interesting range for R is clearly the range below $R = 0.01$.

Note that this model does not allow for the determination of an absolute value $\mathcal{X}$ or τ separately. All that can be measured in the mass spectrometer setup are reaction chances, not reaction coefficients.

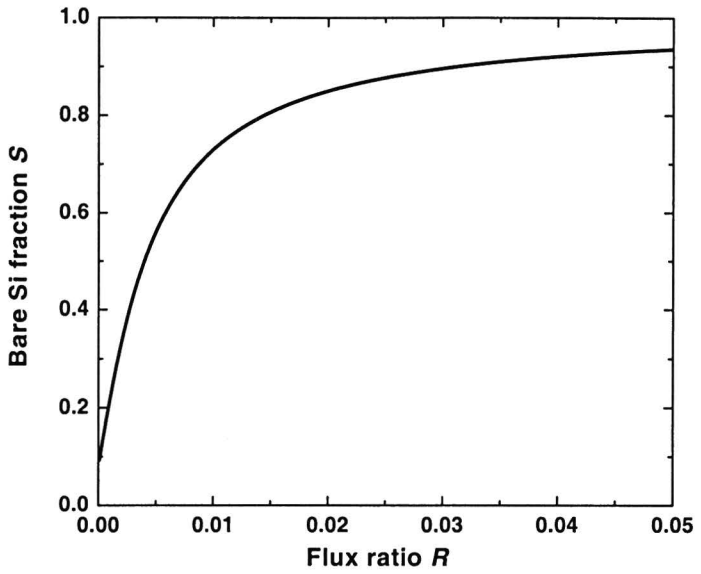

Figure 3.5: The dangling bond fraction as a function of the ion-to-neutral flux ratio R.

Table 3.1: The model parameters needed to describe ion-assisted etching of Si with XeF_2. The ion energy used is 1 keV. Higher energies mean higher sputtering coefficients.

Process	Parameter	Value by		
		Sebel	Vugts	Assumed
Fluorination	$k_s\tau$	0.78	0.71	0.75
Spont. etch	$k_f\tau$	0.084	0.044	0.064
Phys. sputter	p_p	108.3	62.0	85.0
Chem. sputter	p_c	40.0	20.4	30.0

Chapter 4

Article

4.1 Introduction

Plasma etching is the standard etching technique in microelectronics production. Its main advantage is the directionality that is imposed by the ions that bombard the surface of the device [12]. In optimizing plasma etch processes, the main problem one comes across is the tremendous complexity of the plasma environment. This makes it exceedingly difficult to get an understanding of the reaction mechanisms involved.

To circumvent the difficulties associated with plasma etching, many experiments have been performed [3] that give a picture of the processes involved. In several beam etching systems, fairly complete and accurate models have been developed. The system the present work is about has also been studied intensively by etch product analysis [21, 22, 15]. The goal we strive to attain is to apply ellipsometry, a common surface diagnostic in plasma etching, to a beam etching experiment. This in order to narrow the conceptual and experimental gap between plasma etching and beam etching.

In beam etching, only the top atom layer of the sample generates etch products, and therefore only the top atom layer of the sample needs to be considered in the analysis of the results. In ellipsometry, all regions where the laser beam penetrates influence the outcome of the experiments. Therefore it is also necessary to consider deeper regions of the sample. In this region, past the reaction layer, there will be ion damage due to the fact that the 1 keV ions penetrate into deeper layers than the chemical etching agents. Therefore, the envisioned model of the sample surface is that shown in Fig. 4.1: a rough reaction layer that consists of fluorinated silicon species and bare silicon, with damaged amorphous layer beneath it.

Prior to characterizing this two-layer structure, we must understand both layers separately. First, we will describe the composition of the reaction layer by a model from previous experiments in Sec. 4.2, followed by a model of the ion damage in section 4.3. Section 4.4 will be dedicated to detailing our experimental apparatus and measurement techniques. The results of our investigation of the ion damage layer will be presented in section 4.5. In section 4.6, we will investigate the effect of spontaneous etching. Finally, we investigate the ellipsometric behavior of a sample under ion-assisted etching conditions, with a model

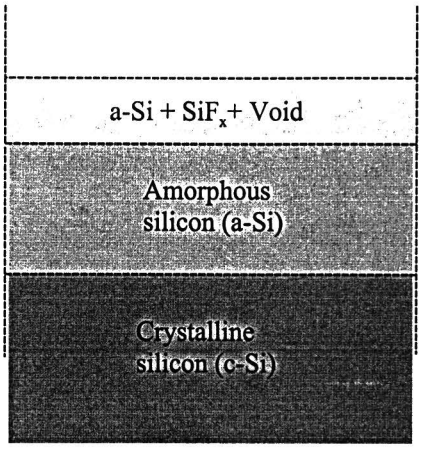

Figure 4.1: Model assumed for the sample surface in ion-assisted beam etching. The ions that are used penetrate further than the reaction layer thickness and cause an amorphous layer to form between the reaction layer and the undamaged substrate.

described in Sec. 4.7 and results in Sec. 4.8. Section 4.9 will be dedicated to concluding remarks.

4.2 Reaction model

Previous research has yielded a reaction model that adequately describes the observed temperature and ion-to-neutral flux ratio dependence at low temperatures. During this research, a physisorbed precursor state of XeF_2 was introduced to explain all observations. To explain the variations in the reactivity of the surface, at least two different species have to be assumed in the surface. These are fluorinated silicon and unfluorinated silicon. We make three further assumptions:

- Temperature dependence is dictated by the evaporation rate of the precursor.
- Composition of the reaction layer is dictated by the ions alone.
- Etching is unaffected by surface roughness.

There are five reaction steps. First, the XeF_2 arrives at the sample surface and is physisorbed into a precursor state that is bound to the surface by Van-der-Waals forces only; some of the XeF_2 evaporates again without reacting. The residence time of the XeF_2 is called τ.

Second, the XeF_2 can react with a bare silicon atom to give a fluorinated silicon atom (reaction coefficient k_s). The XeF_2 can also react with a previously fluorinated silicon atom (reaction coefficient k_f). In this case, SiF_4 is formed, which evaporates.

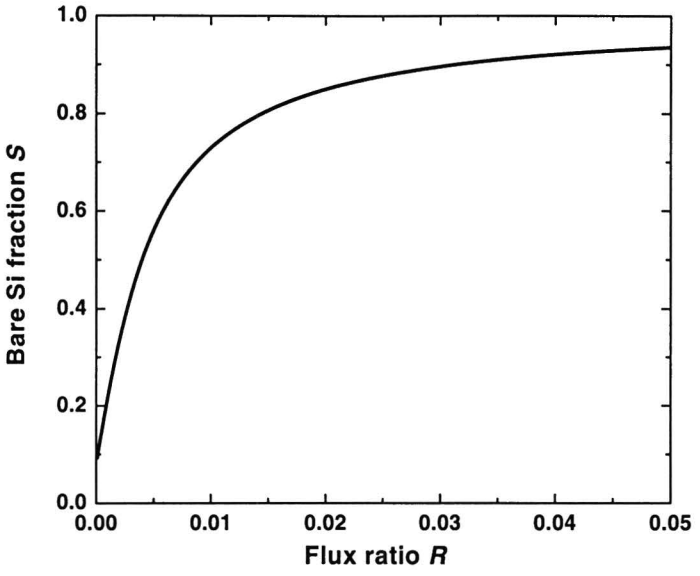

Figure 4.2: The bare Si fraction as a function of the ion-to-neutral flux ratio R.

The final two reactions considered involve the argon ions fired at the sample . The ions can collide with bare Si atoms, which generally does nothing but knock them about. They can also collide with fluorinated silicon species. This can cause direct physical sputtering (probability p_p), or cause the formation of weakly-bound species (probability p_c) [23]. These weakly-bound species will then rapidly evaporate from the sample.

The reaction coefficients have been determined by Vugts *et al* [14] and by Sebel *et al.* [22], using the same experimental setup described in this paper. The values they find differ by a factor of two; the only reaction that remains unaffected is the fluorination of dangling bonds. The only difference between the measurements is in the doping level of the samples. Sebel *et al.* use n-type samples with a resistivity of 30-70 Ω-cm, whereas Vugts *et al.* use samples with a resistivity of only 2-3 Ω-cm. In this work, we use samples with a resistivity of 10 Ω-cm, and will assume reaction coefficients that are the average of those measured by Sebel and Vugts. The reaction coefficients are summarized in Table 4.1.

With this model, the steady-state composition of the reaction layer can be determined as a function of the ion-to-neutral flux ratio R, defined as Ar^+ flux over XeF_2 flux. This relation is shown in Fig. 4.2, where we have plotted the bare silicon fraction $\mathcal{S}$ as a function of R.

4.3 Model of the amorphous layer

We want to understand the influence of ion bombardment on the sample during steady-state etching conditions. The only event we can simulate is the impact

Table 4.1: The model parameters needed to describe ion-assisted etching of Si with XeF_2. The ion energy used is 1 keV. Higher ion energies mean higher sputtering coefficients.

Process	Parameter	Experimental[1]	Experimental[2]	Assumption
Fluorination	$k_s\tau$	0.78	0.71	0.75
Spont. etch	$k_f\tau$	0.084	0.044	0.064
Phys. sputter	p_p	108.3	62.0	85.0
Chem. sputter	p_c	40.0	20.4	30.0

of a single ion into a Si sample, so we start from there.

We consider a small volume element with infinitesimal thickness dz and surface area A (as shown in Fig. 4.3). The surface area A is small enough that the ions falling into the sample will be homogeneously distributed across A, but large enough that $A^{1/2} \gg dz$. In this volume element, a small number d^2N_c of collisions will take place during a small time dt, under the influence of dN_i ions shot into the sample. In mathematical notation:

$$\frac{d^2N_c}{Adzdt} = \frac{d^2N_c}{dN_i dz} \times \frac{dN_i}{Adt}. \tag{4.1}$$

The right hand side has been written like this to show that the number of collisions is proportional to the number of incoming ions. The first term on the right hand side is the chance that an ion will cause a collision at a certain depth z. This can be calculated with the TRIM simulation programme[19]. We introduce the *collision distribution function* $f_c(z)$, for ease of reference:

$$f_c(z) = \frac{d^2N_c}{dN_i dz} \tag{4.2}$$

For one species of ion and sample material, $f_c(z)$ depends only on the ion energy, the angle of incidence, and the depth into the sample. Both terms on the right hand side of Eq. 4.1 are known, so therefore we know all about the way vacancies are generated by the ions. If we now want to know the vacancy distribution in a sample that has a history up to a time t_0, all we have to do is integrate the expression:

$$\frac{dN_c}{Adz} = \int_{-\infty}^{t_0} f_c(z)\frac{dN_i}{Adt}dt. \tag{4.3}$$

The problem we face now is that the effect of a single ion is known only as a function of z, while the integral is over time. The easiest solution is to transform the expression to a z-dependence. As we are interested only in the steady-state distribution, the ion flux does not depend on time. This also implies that the surface moves at a constant velocity v. Using the coordinates defined in Fig. 4.3, we can now write:

$$z - z_0 = -v(t - t_0), \tag{4.4}$$

where the minus sign comes from the fact that the surface is being etched. Substitution into Eq. 4.3 results in:

$$\frac{dN_c}{Adz} = \frac{dN_i}{Adt}\frac{1}{v}\int_z^{\infty} f_c(\zeta)d\zeta. \tag{4.5}$$

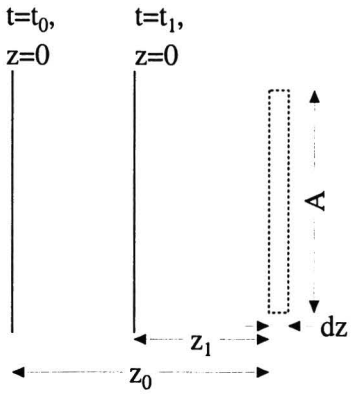

Figure 4.3: The volume element under consideration in the model for the amorphous layer. As the surface is etched, the element moves from depth z_0 at time t_0 to depth z_1 at time t_1. The distribution that is eventually wanted is that of all the damage done since the sample was at $z = \infty$ at time $-\infty$.

Now the integral is easily calculated numerically, the ion flux is known, and all that has to be done is to find an expression for v. In order to do this, we rewrite the etching speed in terms of the number of atoms etched:

$$v = \frac{dN_e}{Adt}\frac{Adz}{dN_0}, \tag{4.6}$$

with N_e the number of atoms etched. The last term on the right hand side is the inverted volume density of Si atoms. The flux of etched atoms is related to the flux of ions bombarding the sample as follows:

$$N_e = N_i \left\{ p_s + \frac{1}{R}\left[\delta_2 + \frac{1}{2}\delta_4\right]\right\} \tag{4.7}$$

In Eq. 4.7, p_s is the number of Si atoms sputtered directly per ion. In the case of one keV Ar^+ ions fired at Si, this probability is 0.588. The second term is the number of atoms that are removed by the ion-assisted etching process. Since for this process the reaction probabilities are known for XeF_2, we can divide by the ion-to-neutral ratio R to determine the effect per ion. The factor one half in front of δ_4 is due to the fact that we are not looking at fluorine reacting, but silicon being etched. Two XeF_2 molecules are needed to form one SiF_4 molecule, whereas only one is needed to form a SiF_2 molecule. Inserting Eq.s 4.6 and 4.7 into Eq. 4.5, we get the total number of collisions in a volume element normalized to the atoms in the element as a function of the depth into the sample:

$$\frac{dN_c}{dN_0}(z) = \frac{R}{Rp_s + \delta_2 + \frac{1}{2}\delta_4}\int_z^\infty f_c(\zeta)d\zeta. \tag{4.8}$$

Finally, we introduce the damage distribution function $F_d(z)$, which is defined as the integral of the collision distribution function over all ζ greater than z:

$$F_d(z) = \int_z^\infty f_c(\zeta)d\zeta. \tag{4.9}$$

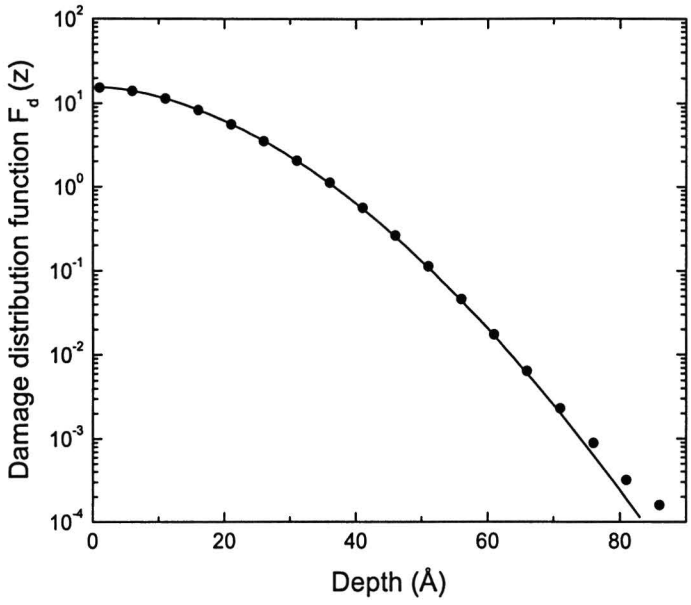

Figure 4.4: Distribution of the vacancy-causing collisions for 1 keV Ar^+-ions impacting upon a pure silicon crystal under a 45 angle.

This allows us to write the number of vacancy-causing collisions per lattice site as

$$\frac{dN_c}{dN_0}(z) = \frac{R}{Rp_s + \delta_2 + \frac{1}{2}\delta_4} F_d(z). \tag{4.10}$$

This model describes the damage distribution in the sample under all constant circumstances.

We performed numerical simulations on the impact of Ar^+ ions under an angle of 45° on crystalline Si. For an ion energy of 1 keV, this result is shown in Fig. 4.4. We curve-fitted a purely empirical function to these data points, assuming:

$$F_d(z) = F_0 \exp\left(-z/r_0\right)^c. \tag{4.11}$$

The fit parameters for various ion energies are listed in Table 4.2. For different energies, the exponent c was found to be nearly constant; the parameters F_0 and r_0 increase with increasing ion energy. From this model, the thickness of the amorphous layer can be determined by stating that the transition from the amorphous to the crystalline phase occurs at a certain critical damage level $F_{d,crit}$. In our model calculations for the ellipsometric response of the sample, we will assume that the sample is amorphous up to the depth where $F_d(z) = F_{d,crit}$.

4.4 Experimental

In this section, we discuss the experimental setup, the quantities we measure, the measurement equipment, the measurement procedures, and finally the influence

Table 4.2: The parameters that result from curve fitting the results of the TRIM simulations for various energies. They are defined in Eq. 4.11. Numbers in parentheses indicate standard deviations resulting from Poisson statistics for p_s, or from fitting for all other quantities.

Energy (keV)	p_s	F_0	r_0	c
0.5	0.335(6)	8.32(2)	13.95(3)	1.86(1)
1.0	0.588(4)	15.64(1)	20.73(2)	1.781(3)
1.5	0.750(4)	25.535(7)	26.49(9)	1.759(1)
2.0	0.864(3)	29.223(5)	31.596(6)	1.7471(8)
2.5	0.959(3)	35.61(1)	36.19(2)	1.751(2)

of imperfections in the vacuum system on the results obtained.

4.4.1 Vacuum apparatus

The setup used has been described extensively in earlier publications [15]. In this section we will only discuss the two modifications that have been made recently. These are the addition of a sample exchange mechanism (depicted in Fig. 4.5) and the addition of an ellipsometer.

The sample holder has been replaced by a rotatable two-slot sample holder. This sample holder has two slots in order to enable the calibration of the mass spectrometer. In its standard position, the sample surface is oriented towards the multiple-beam setup. The sample can be rotated to be in the path of a magnetic linear drive in the vacuum. With this linear drive, the sample can be transported to the load lock. The load lock has a capacity of six samples. Its base pressure is $1 \cdot 10^{-8}$ mbar, achieved by a turbomolecular pump of 56 l/s . It can be sealed off from the main chamber by a valve.

The sample chamber has a base pressure of $5 \cdot 10^{-8}$ mbar and is pumped by turbomolecular pumps. All fluxes impinging on the sample are measured in monolayers per second (ML/s); one monolayer is $6.86 \cdot 10^{18} m^{-2}$, the surface density of Si[100]. The ion flux can be varied from 0 to 0.11 ML/s, and impinges under an angle of 45°. The XeF_2 flux can be varied from 0 to 3.6 ML/s, and impinges under an angle of 52°. The relative orientation of the beams onto the sample is shown in Fig. 4.6.

4.4.2 Ellipsometric theory

This section gives a brief outline of ellipsometry. A full theory can be found in the book by Azzam and Bashara [16]. Ellipsometry is a surface diagnostic that uses the change in ellipticity that a light beam undergoes during reflection at a surface. The Fresnel equations say that reflection coefficients for polarization parallel (R_p) and perpendicular (R_s) to the plane of incidence differ. This is usually expressed as a reflectance ratio ρ:

$$\rho \equiv \frac{R_p}{R_s} \equiv \tan \Psi e^{j\Delta}. \tag{4.12}$$

Equation 4.12 defines the ellipsometric angles Ψ and Δ. The factor $\tan \Psi$ is the ratio of the reflected amplitudes of the p and s waves. The phase difference

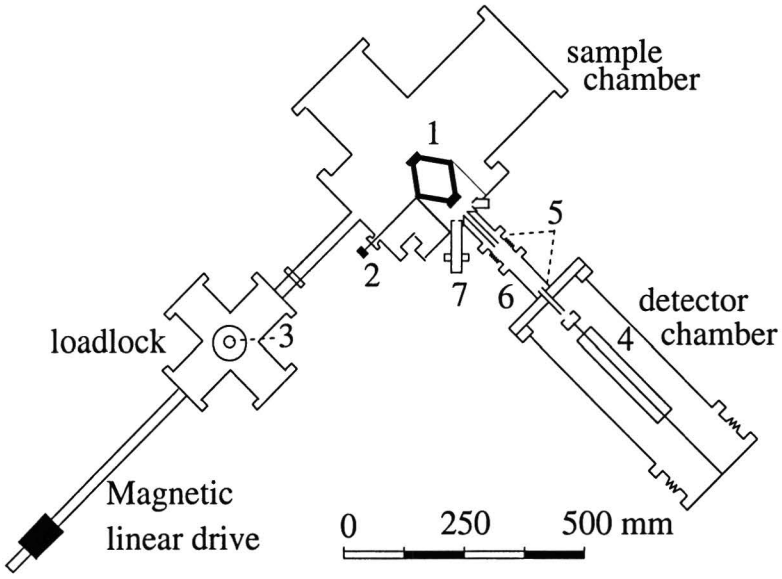

Figure 4.5: The revised setup in horizontal cross-section. The sample is mounted in a rotatable sample holder (1) that can be operated manually via an external drive(2). Samples can be exchanged between the sample holder and the sample storage (3) in the load lock with a linear magnetic drive. The etch products can be analyzed by a mass spectrometer (4) separated from the sample chamber by a double flow resistance (5) and a differential pumping stage (6). The ion gun is also shown (7). The ellipsometer and the XeF_2 molecular beam are out of plane.

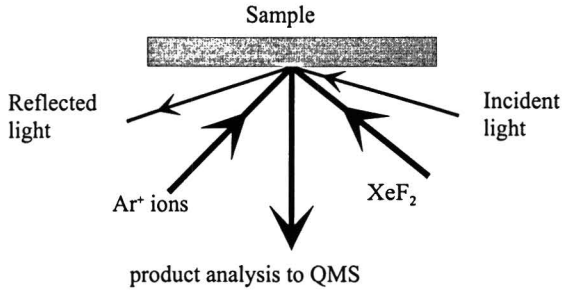

Figure 4.6: The configuration of the various beams in this experiment. The mass spectrometer for etch product analysis will not be used in this work. The incident ellipsometer light is 30° out of plane; the XeF_2 beam is out of plane by 135 degrees.

between the reflected p and s waves is called Δ. Both angles are traditionally expressed in degrees.

The reflectance ratio ρ that is measured depends on the refractive index and the morphology of the surface under investigation, as well as on the wavelength used, the angle of incidence and the presence of thin films on the surface. A medium consisting of a mixture of two different substances (labelled 1 and 2) is modelled as an *effective medium*. The dielectric constant ϵ_r of the effective medium is found by solving the Bruggeman equation [33]:

$$0 = \nu_1 \cdot \frac{\epsilon_{r,1} - \epsilon_r}{\epsilon_{r,1} + 2\epsilon_r} + \nu_2 \frac{\epsilon_{r,2} - \epsilon_r}{\epsilon_{r,2} + 2\epsilon_r}. \tag{4.13}$$

Here the (complex) dielectric constants of media 1 and 2 are called $\epsilon_{r,1}$ and $\epsilon_{r,2}$, respectively. Medium i ($i = 1, 2$) occupies a volume fraction ν_i. Of course, $\sum_i \nu_i = 1$. The complex refractive index of a medium is given by $\epsilon = \tilde{n}^2$. In the case of a rough top layer, medium 1 is vacuum, so $\tilde{n}_1 = 1$.

The interpretation of the measured Ψ and Δ is quite difficult. The Fresnel equations have no easy proportionalities in them. In the case of a substrate with a film on top, all internal reflections in the film have to be taken into account, further complicating matters. This is why the interpretation of the data measured is done by comparison with computer simulations. In this work, a computer program based on the impedance algorithm was used [11]. This allows the interpretation of measurements on substrates that have several thin layers stacked on top of one another. The refractive indices used in the analysis of these measurements are given in Table 4.3.

4.4.3 Ellipsometer

The setup for the ellipsometry is a home-built [5] rotating-compensator ellipsometer (RCE) in the polarizer-compensator-sample-analyzer (PCSA) configuration. The laser light used is linearly polarized 632.8 nm light from a He-Ne laser. Its angle of incidence onto the sample was chosen to be around 74° for maximum sensitivity on silicon. The light is made circular with a $\lambda/4$ retarder.

Table 4.3: Refractive indices used in this work. The value for a-Si is based on experiments that will be described in section 4.5. The value for rough a-Si has been determined from the value for a-Si by applying effective medium theory to a 50/50 a-Si/void mixture.

Material	Assumed $\tilde{n}$
Crystalline silicon (c-Si)	3.882 - 0.02 j [17]
SiO_2	1.457 [18]
Amorphous silicon (a-Si)	4.58 - j 0.72
Rough c-Si (50/50)	2.33 - j 0.01
Rough a-Si	2.643 - j 0.33
Rough SiF_x	1.6 [24]

The polarizer and analyzer used are dichroic sheet polarizers with an extinction coefficient of 10^4. They can both be manually adjusted to within 0.05° of the desired settings.

The rotating compensator is driven by a synchronous motor, with a 2:3 transmission in between for noise suppression. It thus rotates at 33 Hz. An encoding system gives off trigger pulses at every $2\pi/256$ radians. The compensator itself is a zero-order $\lambda/4$ retarder, with a double anti-reflective coating ($R < 0.05\%$). The polarizing properties of the compensator are also expressed in terms of ellipsometric angles Ψ and Δ. For an ideal $\lambda/4$ retarder, these would be $\Psi_c = 45°$ and $\Delta_c = 90°$, respectively. The measured values are $\Psi_c = 45.10 \pm 0.03°$ and $\Delta_c = 89.3 \pm 0.1°$.

The light beam enters and leaves the vacuum through stress-free, non-polarizing quartz windows. It is detected by a photodiode, and amplified. Then it is fed into a 12-bit ADC (resolution 2.44 mV). The ADC is read at every trigger pulse. The resulting signal is Fourier-analyzed in real time by a computer. The resulting values of Ψ and Δ are extracted from the Fourier coefficients. They are averaged over 66 rotations (2 s) for noise suppression, and stored for later analysis.

4.4.4 Measurement procedure

For the pure sputtering and ion-assisted etching measurements, a fixed measurement procedure was followed, which will be described here. The measurement procedure for the spontaneous etching measurements is described in section 4.6.

Before each insertion into the vacuum system the samples were cleaned with alcohol, leaving the native oxide layer in place. Prior to a series of measurements, the plane of incidence onto the sample was calibrated using the native oxide layer, as first done by Smets *et al.* [32] . Subsequently, the compensator was calibrated. The angle of incidence was determined by using the native oxide layer present on the sample. The native oxide layer was found to be 2.7 ± 0.3 nm thick, and the angle of incidence was found to vary between 73.8° and 74.4°. During a measurement run, the compensator was recalibrated once every hour; the plane of incidence was not recalibrated.

4.4.5 Influence of residual gas

In any vacuum system, there is always a residue of gases that have not been pumped out. As turbomolecular pumps are mass selective, the majority of the background gas after a bake-out will consist of hydrogen and helium. The remainder will be species that are introduced into the vacuum in the course of the experiments. So the background gas is a mixture of H_2, He, Ar, and XeF_2. The He and Ar are completely inert, but both H_2 and XeF_2 can dissociate and bind to a bare silicon surface. A residue of XeF_2 will remain in the sample chamber for a long time after an experiment, as it sticks to the walls of the chamber and is released on a long time scale.

The background pressure in our vacuum system is of the order of 10^{-8} mbar. This is equivalent to a particle flux density of the order of 10^{-2} ML/s, about the same as our ion gun current. As the reactive background gases bind to the surface, they form partially fluorinated or hydrogenated species. These are sputtered preferentially by the ions, as they have a lower binding energy to the silicon. This means that the removal rate of the silicon can be enhanced significantly by the background gas. At a background particle flux equal to the ion flux, the dissociating molecules could bind to two Si atoms each, causing the amount of silicon atoms removed per ion (p_s in section 4.3) to increase by two. This is most likely an upper limit. While inconsequential for ion-assisted etching, this process could significantly affect measurements of pure sputtering. We will refer to this process as Background Gas Enhanced Etching (BGEE).

4.5 Sputtering

In this section, we investigate the ellipsometric properties of the sample under pure ion bombardment. We will first examine the dynamical behavior and formation of the amorphous layer, and subsequently go into its steady-state appearance and dependence on ion current.

4.5.1 Time dependence

When a virgin sample is bombarded with ions, there are three processes that occur. This can be seen from Fig. 4.7(a) and (b). One process affects Δ on a timescale of 11 s; another process changes Ψ on a timescale of 20 s. A third long-term process on a timescale of 110 s to 150 s affects both Ψ and Δ.

The fastest process is absent during a transition from one ion energy to another, as can be seen in Fig. 4.7(c) and (d). This leads to the interpretation of this process as the removal of the native oxide layer. This rapid oxide removal lends support to the hypothesis that the top layer in steady state is roughness, and not oxide. The physical cause for this behavior is that silicon oxide has a lower binding energy than silicon itself, and so is sputtered more easily. The second process is the build-up of the damaged layer. This is the part of the damaged layer which is completely amorphous in the steady state. The third and last process is stabilization, and build-up of the damage in the unsaturated boundary layer. We can estimate the amount of time it would take from our model. The total stabilization would occur after the integral in Eq. 4.3 has stabilized. That means that the ions have to have inflicted enough damage on the sample to displace every atom in the amorphous layer at least once. In

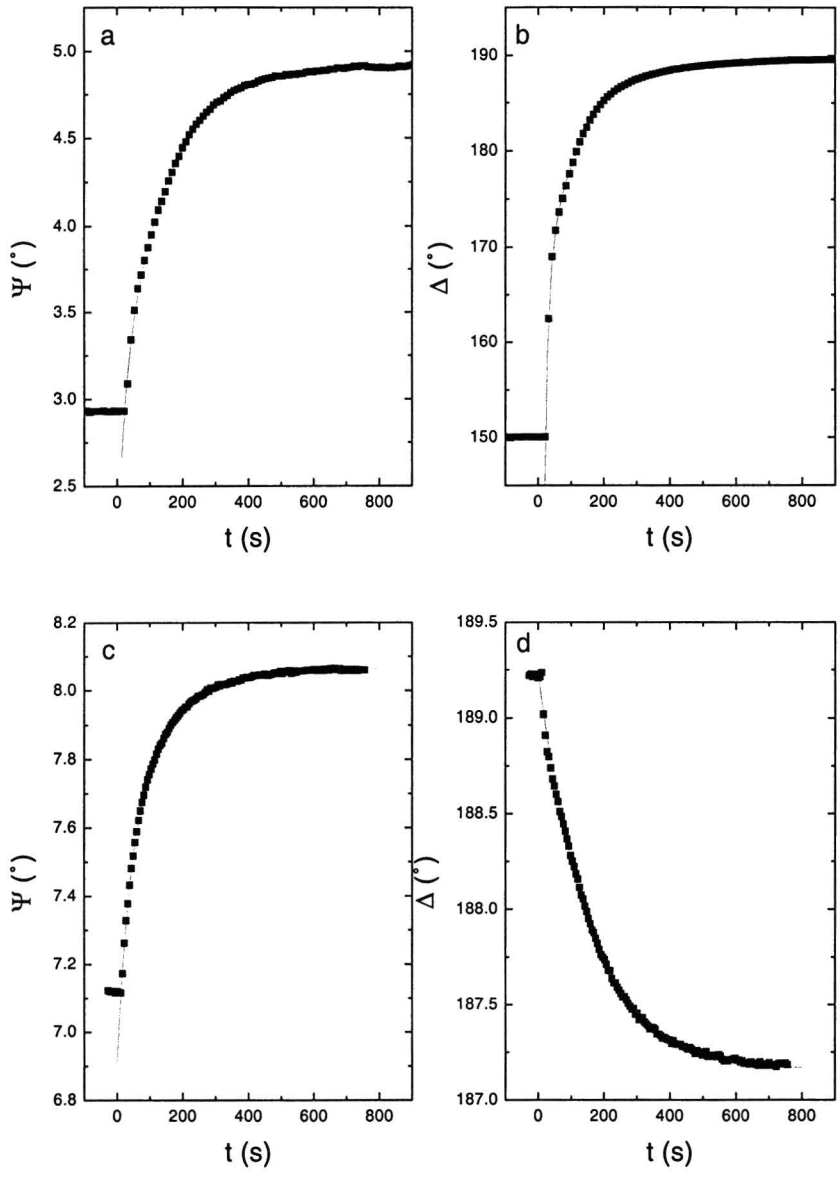

Figure 4.7: The time dependence of the ellipsometric properties of a sample under ion bombardment. The effect the ions have on Ψ (a) and Δ (b) of a virgin sample, starting from native oxide, and that on Ψ (c) and Δ (d) of a sample that is being bombarded with ions of a greater energy than before.

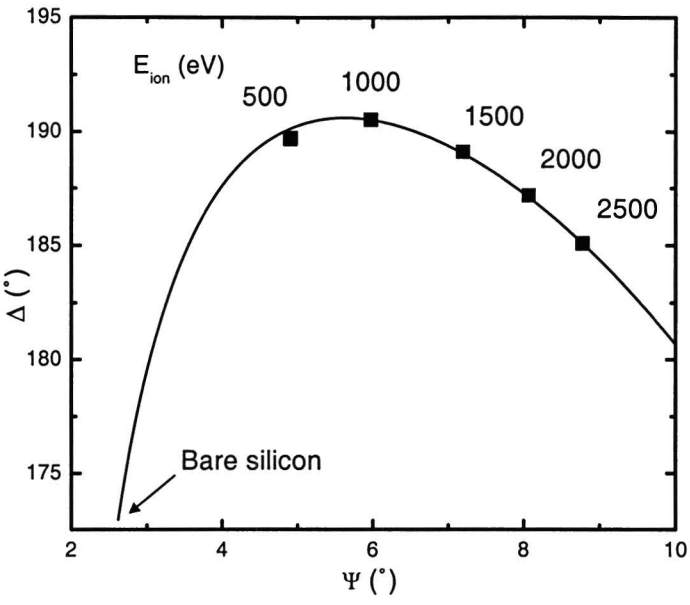

Figure 4.8: Measurement of the steady state values of Si under pure sputtering for various energies. The line represents simulated data for varying damaged layer thicknesses.

a 43 Å layer, there are 30 ML. From the TRIM simulations we know that at 500 eV, an ion displaces 12 atoms on average. For an ion flux density of 0.0165 ML/s, this gives us a time constant of 150 s. This is reasonable agreement with the measured time constant for this long term process.

4.5.2 Steady state

The values of Ψ and Δ measured are shown in Fig. 4.8, along with simulated data. During these measurements the ion current was kept constant at 0.011 ML/s. As can be seen, the agreement of the measurements and the simulations is excellent.

The simulation is based on a two-film model. In this model, the crystalline silicon substrate was covered by an amorphous layer with a thickness that varies with ion energy. On top of the amorphous silicon substrate is a rough top layer of constant thickness. It was assumed to consist of 50 % amorphous silicon and 50 % void. Its refractive index is given by the Bruggeman equation (Eq. 4.13).

The best fit was achieved for a refractive index $\tilde{n} = 4.58 - j0.72$ of amorphous silicon. Throughout the rest of this work, this will be the assumed value for the refractive index. At 20 keV ion energy, Fried *et al.* [20] measured a value of $\tilde{n} = 4.63 - j0.75$. This difference can be accounted for by assuming that the transition between amorphous and crystalline silicon is not completely abrupt. There would be some crystalline silicon left in the amorphous layer. The refractive index we have measured is the solution to the Bruggeman equation for a

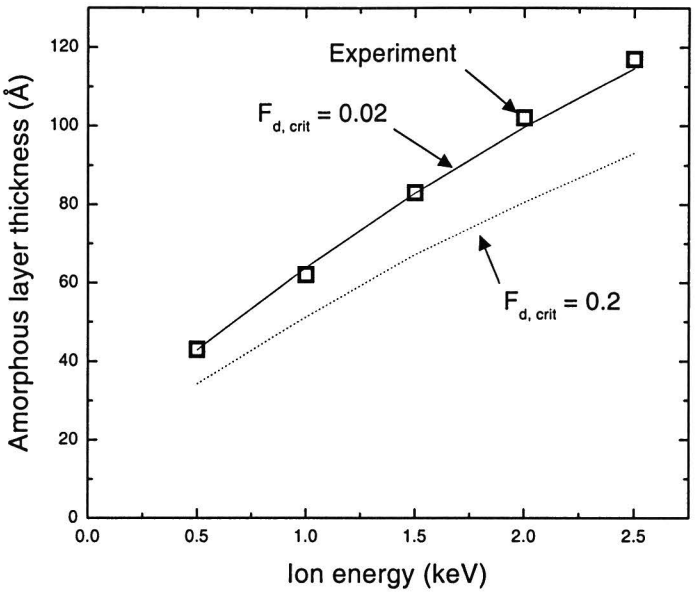

Figure 4.9: Experimental results for amorphous layer thickness as a function of the ion energy. The lines represents the results for simulation with $F_{d,crit} = 0.02$ and $F_{d,crit} = 0.2$.

crystalline fraction of 5%.

The refractive index of the top layer in this case is $\tilde{n}_{rough} = 2.643 - j0.33$. The thickness of the rough top layer was found to have a best fit value of only 3.0 Å. This very small value of the surface roughness can be attributed to the fact that the ions mostly knock silicon atoms about. The atoms then stabilize in energetically favorable positions. In this case, that process would cause the surface to level out on a microscopic scale.

From the simulations, the thickness of the amorphous layer can be deduced. This thickness is plotted in Fig. 4.9, along with the results of TRIM simulations for critical damage levels of 0.02 and 0.2. The $F_{d,crit} = 0.02$ layers are 24% thicker than the $F_{d,crit} = 0.2$ layers. It seems reasonable that there is still a fraction of crystalline silicon left in this layer, corroborating the image constructed before. For $F_{d,crit} = 0.02$, the simulated amorphous layer thicknesses all fall within 2 Å of the measured values. The critical damage fraction that will be used in the remainder of this work is $F_{d,crit} = 0.02$.

The slightly deviating measurement at 500 eV ion energy can be modelled by assuming a rough top layer of 3.5 Å, or alternatively, a minute residue of silicon dioxide could be present due to the relatively small sputtering probability at this energy. A third explanation could be that there is a higher fraction of crystalline silicon in the amorphous layer due to increased boundary layer effects.

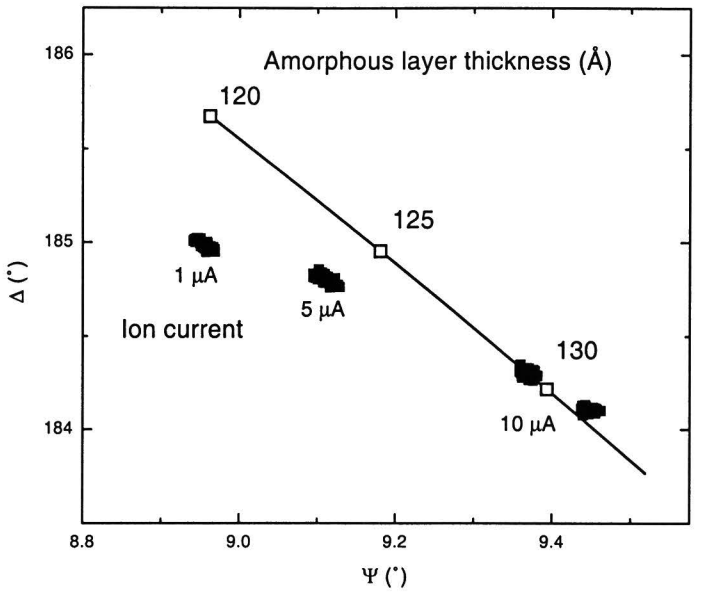

Figure 4.10: The effect of variations in ion gun current on the measured quantities Ψ and Δ (solid squares) at an ion energy of 2.5 keV. The simulation plotted indicates increasing amorphous layer thickness at 5 Åintervals (line and open squares).

4.5.3 Current dependence

The ion current used was also varied; the effect of varying the ion current at an energy of 2.5 keV is shown in Fig. 4.10. Also shown is a simulation of an increase in amorphous layer thickness. It can clearly be seen that the two effects are very similar. This could be the case if the current dependence were caused by an increase in the production of doubly ionized ions (Ar^{++}) in the ion gun. The Ar^{++} would be accelerated to twice the energy of the Ar^{+} ions and cause damage much deeper. In this case, one would expect the double ion concentration to depend on the square of the ion current (which is linear in the ion density in the ion gun). As can be seen in the figure, the effect is about 3.5 times greater for 10 μA ion current than for 5 μA ion current, corroborating this hypothesis.

4.6 Spontaneous etching

The fluorination of the silicon surface was investigated at room temperature. The XeF_2 flux incident on the surface was $\Phi_s(XeF_2) = 2.0$ ML/s. The angle of incidence of the laser light was $\theta_i = 74.2°$. The Si sample was cleaned with HF before it was mounted in the setup. Since a thin oxide layer will remain on the surface after cleaning, the sample was first sputtered by 1 keV Ar^{+} ions with a total dose of 5 ML ($3.4 \cdot 10^{15}$ ions cm^{-2}). Subsequently the ion flux was

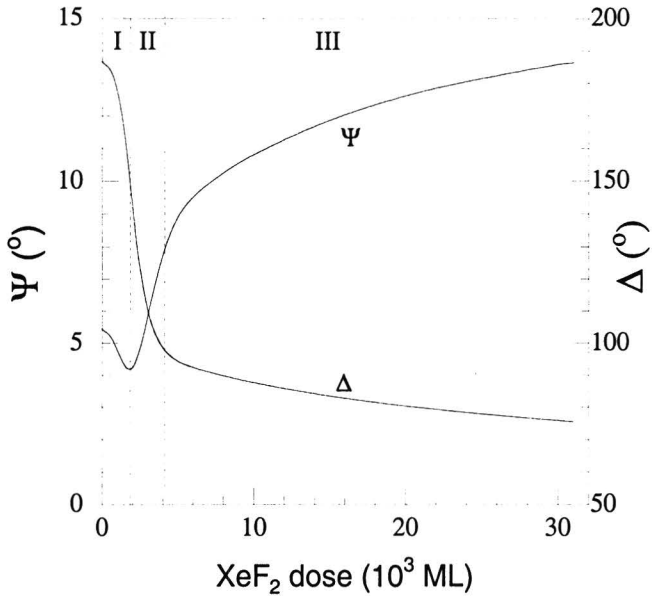

Figure 4.11: Ellipsometric angles Ψ and Δ as a function of the XeF_2 dose. In stage I the amorphous layer is etched simultaneously with the fluorination of the Si which continues in stage II. After a XeF_2 dose of $4 \cdot 10^3$ ML (end of stage II), the ellipsometric angles Ψ and Δ start to decrease much more slowly and a rough Si surface is formed.

switched off and the XeF_2 flux was switched on after 500 s.

4.6.1 Dose dependence

In Fig. 4.11, the results for Ψ and Δ are shown as a function of the XeF_2 dose $\Phi_s(XeF_2)\,t$ at the moment the XeF_2 is turned on ($t = 0$). From the dose dependence, three specific stages are distinguished. After a startup effect, both Ψ and Δ decrease in stage I. In stage II, the value of Ψ increases whereas Δ continuous to decrease rapidly. Finally, in stage III, the value of Δ decreases much more slowly as compared to stage I and II. The angle Ψ shows a similar behavior, but the transition is not very sharp. The deflection point and the start of stage III appears after a XeF_2 dose of $5 \cdot 10^3$ ML.

From the dose dependence of Ψ and Δ, a fast and a slow decrease in Δ was observed (Fig. 4.11). The fast decrease stops after a XeF_2 dose of $4 \cdot 10^3$ ML. This corresponds very well to the dose required to form a steady-state reaction layer [25]. From this we conclude that the fast decrease of Δ is related to the formation of a reaction layer. However, at this point no steady state of Ψ and

Δ is reached which indicates that a second surface process occurs besides the fluorination of the surface. This process becomes dominant beyond a XeF_2 dose of $4 \cdot 10^3$ ML. This is in agreement with the results of Vugts *et al.* [25], who observed severe roughening of the surface for a high XeF_2 dose (up to $5 \cdot 10^5$ ML). From this comparison we thus attribute the slow decrease in the ellipsometric angles to the formation of a rough surface. This is also in correspondence with the results of Aliev *et al.* who observed a similar behavior of Ψ and Δ during fluorination of the surface and subsequent surface roughening in the temperature range $T = 600 - 900$ K [26].

In stage I, the initial decrease in Ψ is explained by the etching of the amorphous layer which was produced during the sputtering of the oxide layer (Sec. 4.5). An accurate calculation of the thickness of the etched layer is difficult because of the startup effect of the XeF_2 and the construction of the reaction layer which results in a lower SiF_4 formation probability. A first-order calculation indicates that about 4 ± 1 nm are etched when the minimum value of Ψ is reached, in reasonable agreement with the values of thickness of the amorphous layer from the previous section. Thus during this period the fluorination of the surface and the removal of the amorphous layer coincide. The best way to avoid this and only measure the fluorination of the surface, is to heat the sample up to 1000 K after the sputtering, which will remove the amorphous layer. However, these temperatures cannot be reached in our setup.

4.6.2 Surface model

In Fig. 4.12 the $\Psi - \Delta$ plot is shown for the total process. The ends of stages I, II, and III are indicated by markers. To describe our measurements, we use a simple model. During the fluorination of the surface, we assume that a uniform SiF_x layer is formed. For the index of refraction we assume $n = 1.60$. Here, the removal of the amorphous layer is not included. After the formation of the reaction layer we assume a rough Si surface is formed with on top of it a SiF_x layer with constant thickness (Fig. 4.13).

The refractive index of a 50/50 mixture of Si and void is $\tilde{n} = 2.33 - j0.01$. The imaginary part of this is too small to show up in our measurements. As we do not know the exact composition of the rough layer, we used the values $\tilde{n} = 2.0$, $\tilde{n} = 2.5$ and $\tilde{n} = 3.0$. The calculated $\Psi - \Delta$ plot for this model is shown in Fig. 4.12 together with the measured $\Psi - \Delta$ plot.

According to the model, the thickness of the SiF_x layer at point 4 is 13 nm (Fig. 4.12). This value is very high compared to the values reported in literature of a reaction layer with a thickness of several monolayers ($0.6 - 1.0$ nm) [28, 29]. Vugts *et al.* reported a fluorine content of the reaction layer of 38 ML for rough surfaces [25]. Assuming an average of two fluorine atoms per Si atom, this corresponds to a SiF_x thickness of about 2.5 nm. This can be regarded as an upper limit in the case of a very rough surface.

There are several possible reasons for the observed discrepancy of the SiF_x thickness. First, we started etching on an amorphous Si layer which might influence the results. Secondly, our model assumes an index of refraction of $n = 1.60$ for the SiF_x layer. In the measurements by Oehrlein, this index of refraction resulted in a SiF_x layer thickness which was within 50% of the XPS values [30]. This indicates that only a rough estimation of the SiF_x layer can be expected from the measurements. The most important reason, however, is

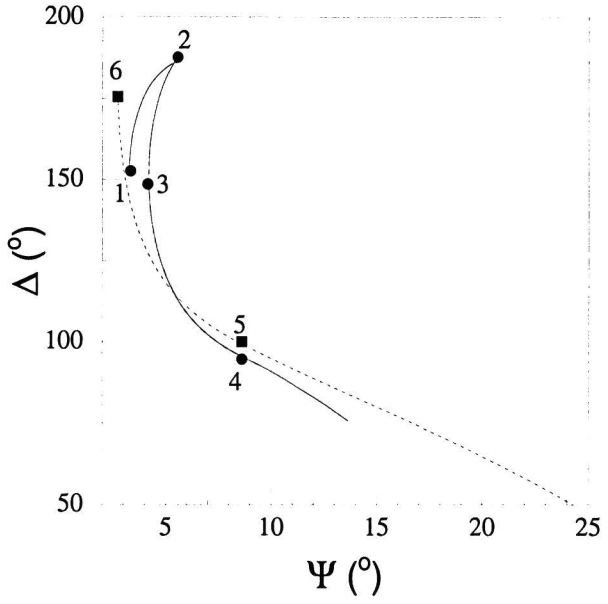

Figure 4.12: Plot of Ψ and Δ during the fluorination of the surface. (1) Ion flux on; (2) the ion flux off and the XeF_2 flux on after 500 s; (3) removal of the amorphous layer (end of stage I); (4) total fluorination of the surface (end of stage II); (5) starting point of model calculation on a clean Si surface; (6) simulation of a steady-state SiF_x layer. Beyond (6), it is assumed that a rough Si surface is formed. The calculated Ψ-Δ behavior is plotted for an index of refraction of $\tilde{n} = 2.0$, $\tilde{n} = 2.5$ and $\tilde{n} = 3.0$.

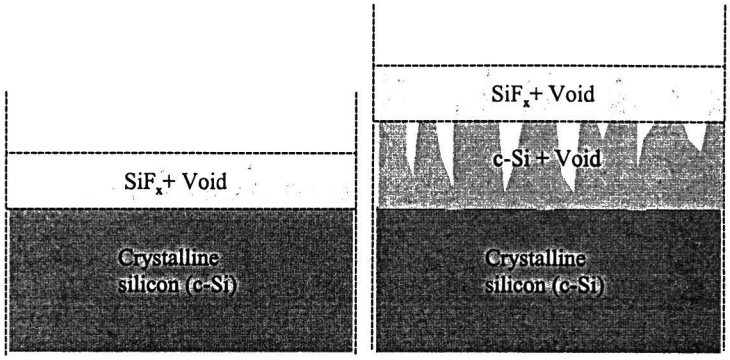

Figure 4.13: Model for the Si surface during fluorination of the surface. For the stages I and II the surface consists of a Si(100) substrate with a uniform transparent SiF_x layer (n =1.60) (left-hand figure). In the next stage the SiF_x layer is assumed constant at 13 nm and a rough Si layer is formed. For the index of refraction of the rough layer various values are used.

that in the results we cannot distinguish between an SiF_x layer and a rough surface. When the rough surface is modeled by an effective layer with the Bruggeman model [Eq. (4.13)] the effective layer will almost be transparent, since the absorption of Si is very small. It is impossible to distinguish between two transparent layers with a thickness on the order of 10 nm. Only for thicker layers, differences in the index of refraction result in a measurable deviation in the corresponding $\Psi - \Delta$ plot.

4.7 Ion-assisted etching: model

In the case of ion-assisted etching, a one-film model cannot suffice to describe the surface because the ions can penetrate up to 100 Å into the sample. The fluorine stays much closer to the surface. Therefore we assume a two-layer model, as shown in Fig. 4.1.

The reaction layer is defined as the layer containing all the fluorine. It is assumed to be homogeneous in order to keep the complexity of the model within reason. The boundary between the reaction layer and the amorphous layer is assumed to be sharp. This assumption is valid as long as the fluorine in the reaction layer stays at the surface. There are two mechanisms that could cause the fluorine to move to greater depths in the sample: thermal diffusion and impacting ions. The thermal diffusion is irrelevant, as the experiment takes place at room temperature. The impacting ions do move the fluorine atoms about, but TRIM simulations have shown that the typical displacement is only about 1 Å. In a typical experiment we etch at least 10 ML of Si for every ML of ions that impacts the sample, so there is no appreciable movement of fluorine into the sample.

The reaction layer is assumed to consist of a mixture of amorphous silicon and SiF_x species. The composition of the reaction layer is assumed to be described by the model detailed in section 4.2.

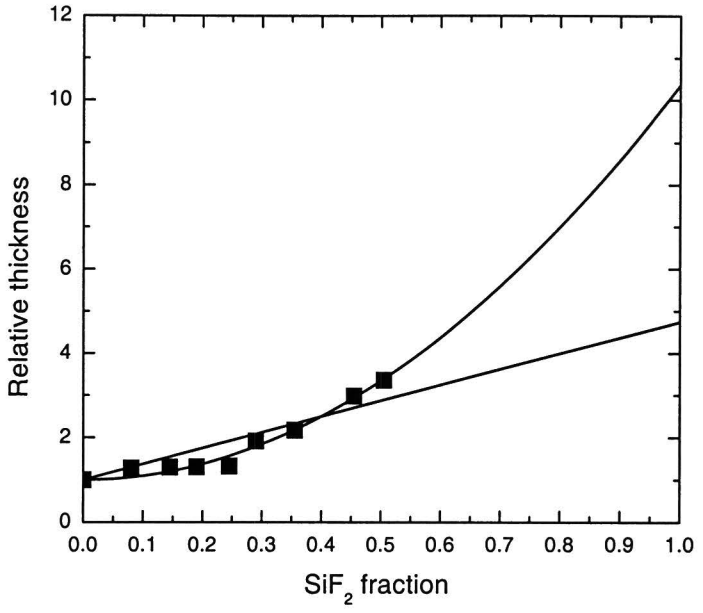

Figure 4.14: Squares: thickness of the partially fluorinated reaction layer simulated by Barone and Graves [23]. It is not immediately clear how to extrapolate these data, and so a linear and a quadratic fit will be tried.

As the composition of the reaction layer is known, we can model its refractive index. The bare silicon is assumed to be amorphous, and have the same refractive index as the rough top layer found in the pure sputtering measurements. The refractive index of the fluorinated species is taken to be the same as was measured in section 4.6.2. We can now use the Bruggeman equation to give us the value of the refractive index of the reaction layer.

Knowing its refractive index, we still need a way to predict its thickness. For very high R, we know that the surface will be much like the top layer in pure sputtering conditions. Therefore, the thickness of the reaction layer under high R will be about 3 Å. The appearance of fluorinated silicon layers under ion bombardment has been simulated by Barone and Graves [23]. From the data produced in these simulations, we can extrapolate a rough fit as shown in Fig. 4.14. The simulations clearly show the effect that the fluorine hinders the silicon bond formation sterically, and that therefore the reaction layer thickness increases with increasing fluorine content. Logically, we expect a linear , but a quadratic fit describes the simulations of Barone better. This results in a lower density for the reaction layer at high fluorine content.

The thickness of the amorphous layer under ion-assisted etching can be determined from the model described in section 4.3. There is only one complication: the stopping power of a thinned-out Si/SiF_x mixture is less than that of an amorphous silicon layer. Therefore, the effective ion-optical thickness of the reaction layer is calculated by taking the total Si content and F content of the reaction layer and multiplying that by the ion-optical cross-sections for Si and

F, respectively. This is then rewritten to an equivalent thickness of amorphous silicon, to be subtracted from the amorphous layer thickness as described in the appendix. We now have a model description for all ellipsometric parameters of the model and can compare it to measurements.

4.8 Measurements

The measurements were performed along a fixed routine. After the calibration measurements described in section 4.4.4, the sample was subjected to pure sputtering with a 0.011 ML/s flux of 1 keV Ar^+ ions. The remainder of the measurement consists of varying the XeF_2 flux onto the sample while it remains under a constant ion bombardment.

4.8.1 Sputtering

From the sputtering measurements, p_s could be determined, as well as the surface roughness in pure sputtering. It was found that, in ion-assisted etching, the measured value was $p_s = 1.8 \pm 0.3$, three times larger than the value found in pure sputtering measurements. The rough top layer increased in thickness from 3 Å in the sputtering measurement runs to 5 Å with residual XeF_2. The time between one ion-assisted measurement and the next was typically one week. This increase in p_s can be explained when one knows that, at the time of the pure sputtering measurements, the vacuum system had not had any XeF_2 introduced to it for about six months. This clearly demonstrates the low removal rate of XeF_2 from the vacuum chamber that is caused by its sticking to the walls. Quantitatively, this effect is roughly the size predicted in section 4.4.5.

4.8.2 Ion-assisted etching

Figure 4.15 shows a measurement run and the best fit of the model to the measurement data. During the measurement, the ion flux was kept constant at 0.011(3) ML/s, and the XeF_2 flux was varied in the range between 4.5 ML/s and 0.2 ML/s after the measurement started at sputtering. As can be seen, the model falls well within the noise range for all R. Sample values for the thicknesses and refractive index of the layers used in this fit are shown in Table 4.4.

Due to the slow response time of the XeF_2 flux, the measured data span some eight hours. The application of the steady state model to these data is justified in Sec. 4.8.4. The dominant source of noise in the measured data is

Table 4.4: Typical values for the model parameters found in the simulations. The bare Si fraction $\mathcal{S}$ determines the composition of the reaction layer and is used to determine its thickness and refractive index. The amorphous layer thickness can then be calculated.

R	$\mathcal{S}$	d_{reac}(Å)	d_{am}(Å)	$\tilde{n}$
10^{-3}	0.22	22.1	24.0	1.74 - j0.04
10^{-2}	0.73	12.9	34.4	2.17 - j0.18
10^{-1}	0.97	4.4	47.0	2.57 - j0.31

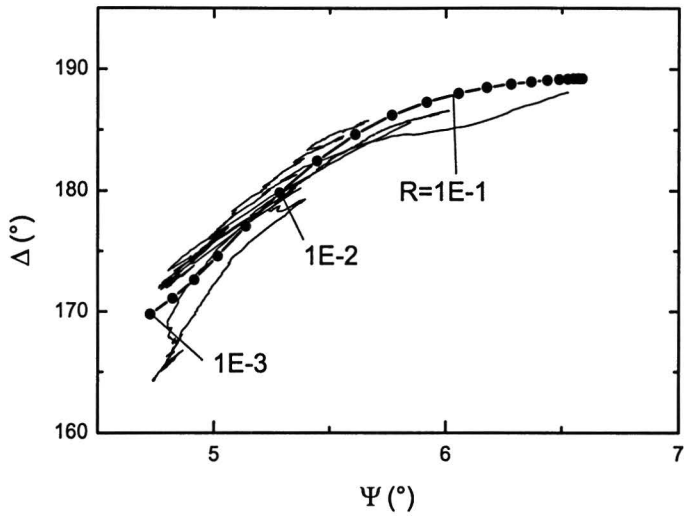

Figure 4.15: Comparison of the measurement data (lines) and the model prediction (dots). The values for ion-to-neutral flux ratio R are also indicated.

the ion gun, which produced a current that could vary by 30 %. This effect is investigated more closely in Sec. 4.8.4.

4.8.3 Model sensitivity

In deriving the model of section 4.7, we have made a number of *a priori* assumptions. We now investigate the necessity of these assumptions. In Fig. 4.16, we compare the best fit from Fig. 4.15 to various models, based on different assumptions. In general, if leaving out an assumption causes the model curve to change, the assumption is proven necessary.

Reaction layer

Figure 4.16(a) shows the effect of not assuming a reaction layer. Clearly, we measure a reaction layer. This figure also justifies the crude interpretation of Ψ as representing the amorphous layer thickness and Δ as representing the reaction layer thickness.

Surface roughness

The effect of assuming a smooth surface is depicted in Fig. 4.16(b). The effect on the amorphous layer is small, as would be expected. The effect on the reaction layer is clear, however. A dense, smooth reaction layer simply does not have the required thickness to have a large effect on Δ. Thus, we can be certain that our sample has a rough reaction layer.

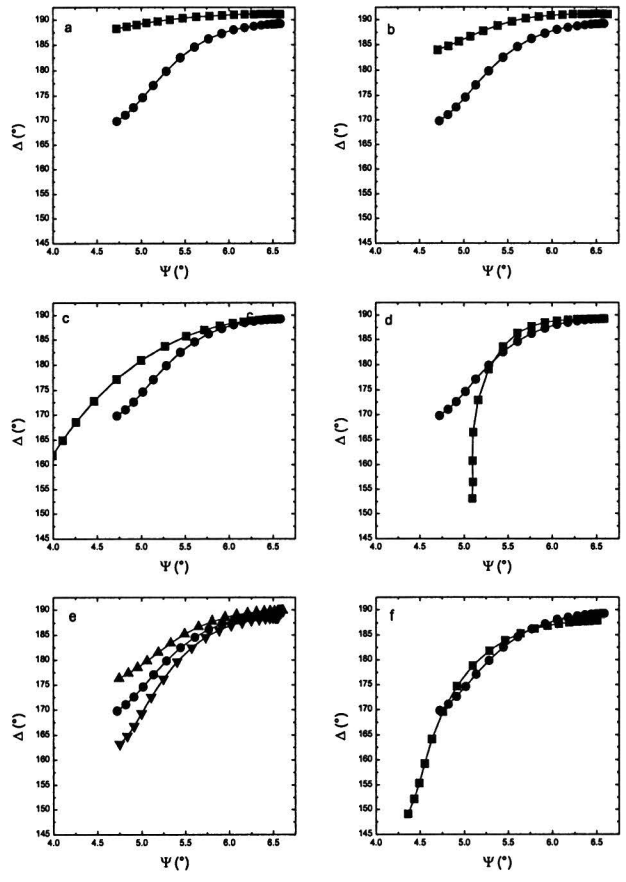

Figure 4.16: The effect on the model prediction of several modelling choices. The circles indicate the model, squares are variants. (a) Presence of a reaction layer. (b) Surface roughness. (c) Reduced density of the reaction layer affects ion stopping. (d) A quadratic fit to the simulation data of Barone. (e) Thickness of the rough top layer during sputtering is 2 Å, 3 Å, or 4 Å, from top to bottom. (f) Background gas enhanced etching does not occur, and therefore the sputtering measurements taken in the ion-assisted etching measurement runs are taken as pure sputtering.

Ion optics

The effect of assuming that the ion-optical stopping power of the reaction layer is the same as that of a similar thickness of amorphous silicon is shown in 4.16(c). As can be seen clearly, the amorphous layer thickness decreases far too rapidly. This effect is due to the increased stopping power of the reaction layer in that model. We find that the difference in stopping powers between the amorphous silicon and the rough SiF_x has to be taken into account.

Fit Barone

The data points calculated by Barone and Graves are few and do not show a clear preference for a linear or quadratic relation of the reaction layer thickness to its fluorine content. Applying a quadratic fit to these data can be seen to have a quite disastrous effect on the correspondence between the model and the measured data, as depicted in Fig. 4.16(d). This is especially valid for low flux ratios, where we work with an extrapolation of Barone's data, maximizing the effect of an incorrect fit.

Reaction layer thickness

The only true fitting parameter in the model for ion-assisted etching is the reaction layer thickness in the sputtering limit. The sputtering measurements from section 4.5 indicate a value of 3 Å, and all the measured data for sputtering in a clean chamber lie in the range 3 ± 1 Å. It is clear that a fit using the value of 5 Åmeasured in a chamber with fluorinated walls would not match the data at all.

Sputtering measurement

Finally, Fig. 4.16(f) shows the effect of using the sputtering measurement of section 4.8.1 to indicate the F_c and the sputtering limit of the reaction layer thickness. The variant model curve in this figure was created using a surface roughness of 5 Å in pure sputtering, neglecting the possibility of BGEE. As can be seen, the agreement is poor, especially in terms of R. The cause for this is a gross misestimation of the processes occurring when $R = \infty$. Especially the silicon removal rate from the surface is badly misjudged, by a factor of three.

Concluding remarks

We conclude that we have developed a model that accurately describes the observed steady-state dependence of ion-assisted etching of silicon with XeF_2 and Ar^+. We have been unable to find any model based on simpler assumptions than ours that can describe the measured data.

4.8.4 Time dependence

A typical measurement run can be seen in Fig. 4.17. The measured quantities Ψ and Δ are plotted as a function of the time. In this measurement, the XeF_2 flux varies from 3.25 ML/s on the outset to 0.16 ML/s at the end of the measurement. This variation in XeF_2 flux was achieved by instantaneously

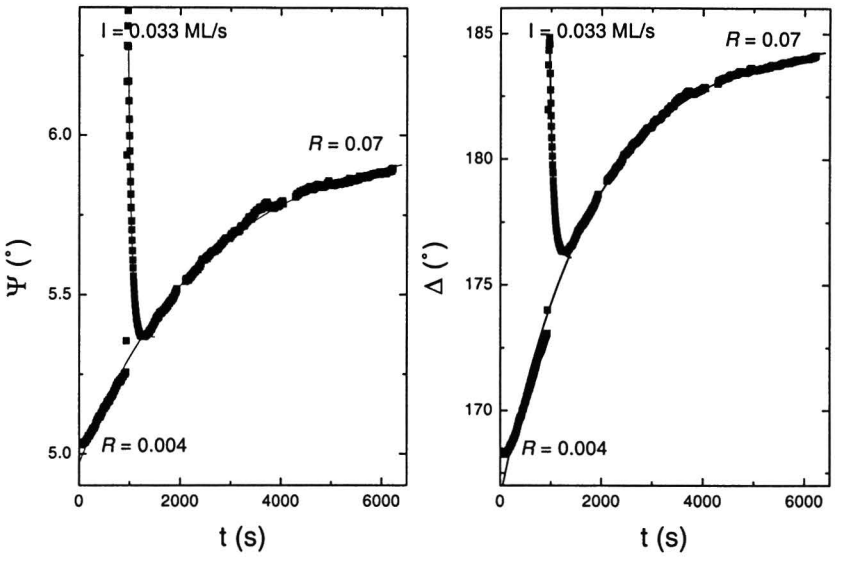

Figure 4.17: The time dependence of ion-assisted etching. Clearly, processes occur on two different timescales.

increasing the power with which the XeF_2 reservoir was cooled. The ion flux was peaked briefly at 0.033 ML/s from its usual level of 0.011 ML/s.

The processes have been fitted with an exponential decay curve, yielding a time constant of $1.83(1) \times 10^3$s for the slow process governing Ψ, and $2.51(2) \times 10^3$s for Δ. The difference in the time constants can be explained by the generally nonlinear dependence of Ψ and Δ on the flux ratio R. The length of the timescales involved here can be explained by taking into account the extremely slow response of our XeF_2 source. Adjusting the XeF_2 flux requires the XeF_2 crystal adjust to the new temperature, a process that takes about five minutes. The main cause of the slow response is the time taken for restoration of the vapor/solid balance in the holder and the 0.8 m of tubing from the holder to the capillary. This process apparently takes about an hour, causing the slow response of the system.

The response of the system to a change in ion current is much swifter, as can also be seen in Fig. 4.17. The surface takes about 0.6 ML of ions to respond to an increase in ion current. This is valid for both Ψ and Δ. A more accurate investigation of the time response will have to be made later on. The response to a decrease in ion current is slower and can therefore be analyzed with the current data.

The response in Ψ predominantly represents the change in thickness of the amorphous layer. This thickness depends on R, and is also influenced by the double ionization at higher ion currents as described in section 4.5. The time it would take the damaged layer to revert to its 'original' state would be determined by the time needed to etch away the extra thickness of the ion damaged layer. This would depend on the value of this extra thickness, the ion current and the etch rate, causing a complex behavior that would need to be investigated

further.

The response in Δ can be interpreted crudely as the response of the reaction layer thickness and composition. This balance appears to have a constant restoration rate over a large range of R, so it is suspected that this process is induced by the ions. In terms of ion dose, the restoration dose is about 0.8 ML for the disturbance shown in Fig. 4.17.

The fact that the time response of the XeF_2 source is an order of magnitude slower than the adjustment of the surface of the sample to changing circumstances means that we can assume that the reaction layer is in steady state throughout the measurement. This means that the measurements of a sweep in XeF_2 flux can be used for comparison with the model developed in section 4.7, which assumed steady state.

4.9 Concluding remarks

We have installed an ellipsometer onto our beam etching setup in an attempt to bridge the gap between beam etching and plasma etching. We have used it to measure the ellipsometric properties of a Si sample during Ar^+ sputtering, spontaneous etching, and ion-assisted etching. This is an important first step in bridging the gap between plasma etching and beam etching.

The sputtering measurements could be modelled satisfactorily with a two-layer model. The amorphous layer thickness could be described consistently and satisfactorily with TRIM simulations, and surface roughness was found to be limited to 3 Å. Background gas enhanced etching (BGEE) was found to have a significant influence on our sputtering measurements.

Spontaneous etching was also investigated and it was found that the measurements could be described by a rough reaction layer about 13 nm thick, and a rough silicon layer underneath that grows slowly with time.

For ion-assisted etching, we have devised a two-layer model that satisfactorily explains the observed behavior with only a single fit parameter: the reaction layer thickness. The refractive index of the reaction layer can be determined with a Bruggeman-modelled mixture of rough amorphous silicon and rough SiF_x. The thickness of the reaction layer matches a linear extrapolation of molecular dynamics simulations by Barone and Graves [23].

Future research options would include background gas analysis for a better characterization of BGEE and a real time measurement of R. We could also obtain a higher measurement quality by stabilizing the ion gun. Other research possibilities are the investigation of the effect of doping on etching processes, and the temperature dependence of the reaction layer appearance.

4.9.1 Acknowledgements

The authors would like to M. J. de Koning and L. H. A. M. van Moll for designing and installing the sample exchange mechanism and the ellipsometer, D. H. A. Driessen for calibrating the ellipsometer, and M. C. M. van de Sanden for stimulating discussions.

Bibliography

[1] P.G.M. Sebel, Dynamics of ion-assisted etching, PhD thesis, Eindhoven University of Technology (1999).

[2] P.R. Larson, K.A. Copeland, G. Dharmasena, R.A. Lasell, M. Keil, M.B. Johnson: Atomic fluorine beam etching of silicon and related materials. JVST B, vol. 18, 307 (2000).

[3] H.F. Winters and J.W. Coburn, Surface science aspects of silicon etching, Surf. Sci. Rep., vol. 14, 161 (1991).

[4] M.J.M. Vugts, Reaction layer dynamics in silicon etching. PhD thesis, Eindhoven University of Technology (1995).

[5] W.J. Mestrom, Ellipsometrie bij bundeletsen, MSc thesis VDF/NO 99-07, Eindhoven University of Technology (1999).

[6] D.H.A. Driessen, Calibratie roterende compensator ellipsometer-opstelling, traineeship report VDF/NO 97-12, Eindhoven University of Technology (1997).

[7] F.L. Pedrotti and L.S. Pedrotti, Introduction to optics, 2nd edition. Prentice-Hall International, Inc., New York (1993).

[8] G.M.W. Kroesen, Ellipsometrie. Collegedictaat VDF/NG 96-01, Eindhoven University of Technology (1996).

[9] D.J. Griffiths, Introduction to electrodynamics.

[10] H.A.J. Senhorst, Etching studies in a multiple-beam surface experiment. PhD thesis, Eindhoven University of Technology (1990).

[11] G. M. W. Kroesen, G. S. Oehrlein, E. de Frésart, and M. Haverlag, J. Appl. Phys. **73**, 8017 (1993).

[12] J. W. Coburn and H. F. Winters, J. Appl. Phys. **50**, 3189 (1979).

[13] M. J. M. Vugts, L. J. Hermans, H. C. W. Beijerinck, J. Vac. Sci. Technol. A, **14**, 2820 (1996).

[14] M. J. M. Vugts, L. J. Hermans, H. C. W. Beijerinck, J. Vac. Sci. Technol. A, **14**, 2138 (1996).

[15] M .J. M. Vugts, G. J. P. Joosten, A. van Oosterum, H. A. J. Senhorst, and H. C. W. Beijerinck, J.Vac.Sci.Technol. A, **12**, 2999 (1994).

[16] R. M. A. Azzam and N. M. Bashara, *Ellipsometry and polarized light*, North-Holland, Amsterdam (1992).

[17] E. D. Palik (ed.), *Handbook of optical constants, vol. I*, 547-569, Academic Press (1998).

[18] E. D. Palik (ed.), *Handbook of optical constants, vol. I*, 749-763, Academic Press (1998).

[19] J. F. Ziegler, J. P. Biersack, and U. Littmark, *The stopping range of ions in solids*, 109-140, Pergamon, Oxford (1985).

[20] M. Fried, T. Lohner, E. Jároli, Gy. Vizkelethy, G. Mezey, J. Gyulai, M. Somogyi, and H. Kerkow, *Thin solid films*, **116**, 191 (1984).

[21] P. G. M. Sebel, L. J. Hermans, and H. C. W. Beijerinck, J. Vac. Sci. Technol. A **18**, 2759 (2000).

[22] P. G. M. Sebel, L. J. Hermans, and H. C. W. Beijerinck, J. Vac. Sci. Technol. A **17**, 3368 (1999).

[23] M. E. Barone and D. B. Graves, J. Appl. Phys. **77**, 1263 (1995).

[24] G. S. Oehrlein, J. Vac. Sci. Technol. A **11**, 34 (1993).

[25] M. J. M. Vugts, M. F. A. Eurlings, L. J. F. Hermans, and H. C. W. Beijerinck, J. Vac Sci. Technol. A **14**, 2780 (1996).

[26] V. S. Aliev and V. N. Kruchinin, Surf. Sci. **442**, 206 (1999).

[27] M. M. Ibrahim and N. M. Bashara, Surf. Sci. **30**, 632 (1972).

[28] B. Roop, S. Joyce, J. C. Schultz, and J. I. Steinfeld, Surf. Sci. **173**, 455 (1986).

[29] F. R. McFeely, J. F. Morar, and F. J. Himpsel, Surf. Sci. **165**, 277 (1986).

[30] G. S. Oehrlein, Surf. Sci. **386**, 222 (1997).

[31] N. Matsunami, Y. Yamamura, Y. Itakawa, N. Itoh, Y. Kazumata, S. Miyagawa, K. Morita, R. Shimizu, and H. Tawara, At. Data Nucl. Data Tables **31**, 1 (1984).

[32] A. H. M. Smets, D. C. Schram, and M. C. M. van de Sanden, J. Appl. Phys. **88**, 6388 (2000).

[33] D. A. G. Bruggeman, Ann. Phys. **24**, 636 (1935).

Appendix A

Software

The ellipsometric model simulations done in this work employed home-written software. The listings are provided in the following. A MAPLE worksheet was used to calculate the composition of the reaction layer, as well as the thickness of both the reaction layer and the amorphous layer. These data were saved to a file called `temp`, which was read by the Pascal programme `n2psidel`. This programme invokes the leg_ei procedure from the `ellsim` package developed for ellipsometric studies by Kroesen *et al.* [11]. The output of the program is a file of R values and matching (Ψ-Δ) values for two situations. One is for the case of just an amorphous layer and no reaction layer, and the other one is for the case of amorphous layer and reaction layer both.

A.1 Reaction layer simulation

For the calculation of the ion-optical stopping power of the reaction layer, the stopping powers of F and Si for impacting Ar^+ must be known. The values of these (electronic) stopping powers are taken from Matsunami [31], who uses a Lindhard approximation.

The reaction layer is assumed to contain a constant amount of silicon, which can be fluorinated. The ion-optical cross-section of the silicon in the layer is known from the sputtering measurements. All that is needed is a way to process the influence of the added fluorine in the layer. This is done as follows:

$$d_{opt} = \frac{1}{2} \times d_{sput} + \frac{1}{2} \times d_{sput} \times 2 \times \mathcal{F} \times \frac{\sigma_{\mathrm{F}}}{\sigma_{\mathrm{Si}}}. \tag{A.1}$$

Here, d_{opt} is the thickness of amorphous silicon with the same stopping power as the reaction layer, d_{sput} is the thickness of the rough top layer measured during sputtering, $\mathcal{F}$ is the fraction of Si atoms that have been fluorinated. The factors 1/2 are due to the fact that the reaction layer is 50 % vacuum, the factor 2 due to the fact that every fluorinated Si atom has two F atoms attached to it.

```
restart:
Reff:=(R,E)->R*sqrt(E):
Eq:=(1-Reff(R,E)*(1-Si)*0.5*p[ch])*
  (Si*kappa[s]-(1-Si)*kappa[f]) = Reff(R,E)*(1-Si)*0.5*
  (p[ph]+p[ch])*(1+Si*kappa[s]+(1-Si)*kappa[f]):
```

```
E:=1: N[0]:=15.72: r:=20.64: c:=1.75: p[sput]:=3*0.588:
p[ph]:=85: p[ch]:=30: kappa[s]:=0.75: kappa[f]:=0.064:
a:=2.643-0.33*I: b:=1.6: F[0]:=0.02: dinf:=3:
A1:=p[ph]/(2*kappa[f]):
B1:=p[ch]/kappa[f]:
C1:=(kappa[s]+kappa[f])/(2*kappa[f]*kappa[s]):
D1:=(p[ph]+p[ch])/(2*kappa[s]*kappa[f]):
delta[2]:=A1*Reff(R,E)/(C1 + D1*Reff(R,E)):
delta[4]:=(1 + B1*Reff(R,E))/(C1 + D1*Reff(R,E)):
z[0]:=R->r*(-ln(F[0]/N[0]*(p[sput] + (delta[2] +
  (1/2)*delta[4])/Reff(R,E))))\^(1/c):
stemp:=[solve(Eq, Si)]:
if limit(stemp[1], R=infinity)>0 then S:=R->stemp[1]
  else S:=R->stemp[2] fi:

ascfile := fopen(temp, WRITE, TEXT):
for i from 0 to 20 do
  R:=evalf(10\^(-3+0.2*i)):
  reactdikte[i]:=2*dinf*(0.5+3.75*(1-(S(R)))):
  optdikte[i]:=0.5*dinf*(1 + 1.8*(1- S(R))):
  amorfdikte[i]:=z[0](R)-optdikte[i]:
  if amorfdikte[i]<0 then amorfdikte[i]:=0 fi:
  v:=evalf(S(R)): w:=(1-v):
  brug[i]:=2*sqrt(-(v + w)*(-2*v*a^2 + v*b^2 - 2*w*b^2 + w*a^2-
    sqrt(4*v^2*a^4 + 4*v^2*a^2*b^2 + 26*v*a^2*w*b^2 -
    4*v*a^4*w + v^2*b^4-4*v*b^4*w + 4*w^2*b^4 + 4*w^2*b^2*a^2
    + w^2*a^4)))/(4*v+4*w);
  writedata(ascfile, [[R, Re(brug[i]), Im(brug[i]),
    reactdikte[i]/10, amorfdikte[i]/10]]);
od:
close(ascfile);
```

A.2 Ellipsometry simulation

```
Program n2psidel;

 { This program calculates the (psi, delta) data points  }
 { from the refractive indices and thicknesses           }
 { given in the temp file and exports them to a data     }
 { file of your choosing.                                }

uses dos, crt, ellunit;

var psitemp, deltatemp, renl, imnl, dl: layers_array;
    R, Renreac, Imnreac, dreac, damorf,
      psia, dela, psir, delr: array [0..100] of real;
    lambda, phi, rensub, imnsub: real;
    imax, i, ntlagen: integer;
    inputfile, outputfile: string;
```

```
    begindata, opslag: text;

begin

     {Some constants}

 lambda:=632.8;
 rensub:=3.882; imnsub:=-0.019; {Substrate refractive index}
 renl[0]:=4.58; imnl[0]:=-0.72; {Amorphous layer refractive index}
 ntlagen:=2; inputfile:='temp';
 write('What angle of incidence?   '); readln(phi);
 write('What output file? '); readln(outputfile);

     {Read the temp file}

assign(begindata, inputfile); reset(begindata); i:=0; while not
eof(begindata) do
  begin
    i:=i+1;
    readln (begindata, R[i], Renreac[i], Imnreac[i],
      dreac[i], damorf[i]);
  end;
imax:=i;

     {Do the calculations}

for i:=1 to imax do
 begin
  renl[1]:=Renreac[i]; imnl[1]:=Imnreac[i]; dl[1]:=dreac[i];
  dl[0]:=damorf[i];
  leg_ei(psitemp, deltatemp, ntlagen, lambda, phi,
    rensub, imnsub, renl, imnl, dl);
  psia[i]:=psitemp[0]; dela[i]:=deltatemp[0];
  psir[i]:=psitemp[1]; delr[i]:=deltatemp[1];
  writeln(psitemp[0]:8:3, '   ', psitemp[1]:8:3, '    ',
    deltatemp[0]:8:3, '    ', deltatemp[1]:8:3);
 end;

     {Create the output file}

assign(opslag, outputfile); rewrite(opslag); writeln(opslag,' R
Psi_a      Delta_a    Psi_r      Delta_r'); for i:=1 to imax do
 begin
  writeln(opslag, R[i]:8:5, '   ', psia[i]:8:5, '   ',
    dela[i]:8:4,     '   ', psir[i]:8:5, '   ', delr[i]:8:4);
 end;
close(opslag);
readln;

end.
```

Appendix B

Technology assessment

One of the key processes used in the semiconductor industry is etching. Investigations into the mechanisms of etching in actual plasma etching reactors are difficult, as the plasma environment is extremely complicated. This limitation is circumvented by using a beam etching setup to investigate the etching process.

However, a beam etching setup has its own disadvantages, and the most serious of those is the huge difference in both experimental environment and conceptual framework. The most common diagnostic technique in plasma etching is ellipsometry. By the application of this technique to beam etching, this work has helped narrow the disparity between plasma and industry on the one hand etching and beam etching and science on the other hand.